Eindhoven University of Technology

MASTER

Design of a Large Stroke Two DoF Translation Stage Based On Compliant Joints

Koese, B.

Award date:
2021

Link to publication

Design of a Large Stroke Two DoF Translation Stage Based On Compliant Joints
Master thesis

Bart Koese

January 29, 2021
Eindhoven, the Netherlands

Report number: DC 2021.011

Design of a Large Stroke Two DoF Translation Stage Based On Compliant Joints

Master thesis

by

Bart Koese

Preface

This report is the outcome of a graduation project that has been carried out at Sioux Technologies to obtain the degree of Master of Science at the Dynamics and Control group of the Eindhoven University of Technology. This project is about the design of a two degree of freedom translation stage that uses large stroke compliant joints to achieve motion. During this project, I learned a lot about the wonderful world of compliant mechanisms, their amazing properties, and the creative compliant mechanism designs that exist.

First, I would like to would like to say special thanks my TU/e coach Paul Vrankcen for the excellent guidance. I really enjoyed the Thursday morning meetings. Not only did I receive improvements for my own project, I learned a lot about many other great projects.

Next, I want to thank my coach from Sioux Technologies: Freek Fennis. Freek, thank you for are your wise lessons, all the effort you put into helping me each week, and for your patience. I really enjoyed working with you.

Finally, I would like to thank my family and my girlfriend in supporting me during all my years of studying. You have been great!

Summary

Compliant joints are frequently used in accurate positioning systems due to their advantageous properties such as the absence of backlash, friction, and wear. The use of these mechanisms is typically limited to short stroke applications, mainly due to stress and stiffness loss. However, multiple studies showed that compliant joints can be used in large stroke applications. Various systems designed by Sioux Technologies, the initiator of this project, can significantly benefit from the use of large stroke compliant joints. Consequently, Sioux Technologies created this project with two goals: first, to obtain a design method for large stroke compliant joints used in accurate motion systems. Second, to identify critical and practical design aspects and potential risks for implementing large stroke compliant joints in these systems. To obtain, test, and demonstrate these aspects, Sioux Technologies specified a case study with challenging requirements. This case study involved designing a large stroke two degree of freedom translation stage that is entirely guided by compliant joints.

The results from this project can be divided in two parts. The first part comprises the theoretical aspects of the design of the compliant joints. A design method has been obtained with which the geometries of different compliant joints are optimized to obtain high static and dynamic performance. This method uses an optimization algorithm in combination with finite element method software to obtain optimal geometry parameters for a given joint.

The second part is the practical design of the translation stage that followed from this thesis. The translation stage designed in this thesis consist of two actuated compliant rotational joints and two arms. Compliant joints have been optimized for this mechanism, which deflect at a maximum angle of $\pm 30°$. Furthermore, the translation stage is driven by two linear ironless motors. To determine the position of the actuator, two linear magnetic encoders have been used which measure the angle of the joints. The main takeaways of the design of the translation stage are as follows: first, a stiff and lightweight design has been made for static and dynamic performance of the system and to minimize the joint loads. Next, the benefits of the compliant (e.g. no friction or play) joints have been maintained by, for example, using actuators that do not require tribological contacts and using contactless sensors.

Contents

Nomenclature

Symbols

Symbol	Description	Unit
a	acceleration	[m/s^2]
E	Young's Modulus	[GPa]
f_2	second eigenfrequency	[Hz]
g	gravitational constant	[m/s^2]
G	shear modulus	[GPa]
H, h	height	[m]
J	inertia	[kg/m^2]
l	length	[m]
m	mass	[kg]
M	Moment	[N m]
R	fatigue strength to Young's modulus ratio	[-]
R_{m}	ultimate tensile strength	[MPa]
s_x, s_y	stroke in the x and y direction	[mm]
t	thickness	[m]
T	kinetic energy	[J]
V	potential energy	[J]
v	velocity	[m/s]
θ	rotation about the z-axis	[rad]
ρ	volumetric mass density	[kg/m^3]
σ	stress	[MPa]
σ_{f}	fatigue strength	[MPa]
τ	torque	[N m]

Abbreviations

CAD	computer aided design	FEM	finite element method
CoM	center of mass	FFCH	five-flexure cross hinge
CWH	cartwheel hinge	INFH	infinity hinge
DoF	degree of freedom	PECM	precision electro chemical machining
EDM	electrical discharge machining	TFCH	three-flexure cross hinge
e.g.	exempli gratia (for example)	TU/e	Eindhoven University of Technology
FDM	fused deposition modelling		

1.   Introduction

1.1   Sioux Technologies and compliant joints

Sioux Technologies is a research and development company with competences in mathware, software, electronics, assembly, and mechatronics. The mechatronics department is specialized in designing highly accurate positioning systems for various markets such as the semiconductor, analytical, medical, and printing industry.
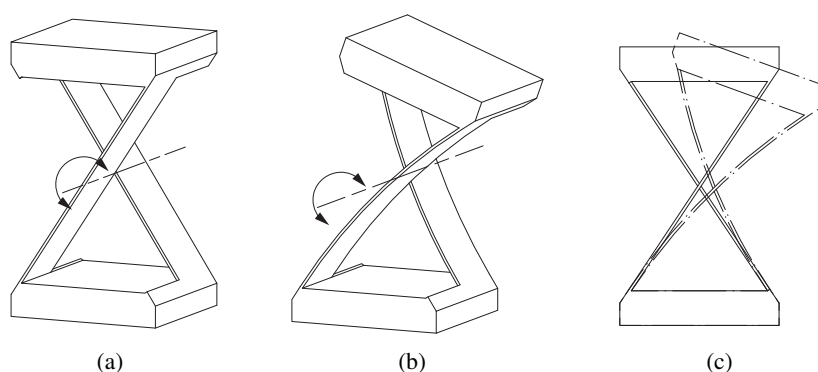
Figure 1.1: Cross spring pivot [1] compliant joint: (a) undeflected state, (b) rotated state, (c) overlay view

In these systems, compliant joints (also called compliant hinges or flexures) are frequently used as they can provide several key advantages over traditional sliding or rolling based joints. Compliant joints are mechanisms that achieve motion by means of elastic deformation [2], an example of which is shown in Figure 1.1. These joints behave highly predictably as they are free from backlash, friction, wear, and vibrations caused by rolling or sliding elements [3, 4]. Furthermore, flexures are contamination free as they do not generate particles from friction and they do not require lubricants that can evaporate in vacuum environments [5]. Although there are many benefits to compliant joints, their use is typically restricted to small-stroke applications. Subjecting a flexure to large deformations can lead to high stress (material failure) and loss of support stiffness, which deteriorates static and dynamic performance [3, 6, 7]. In addition, these joints often suffer from parasitic motions, as they do not always translate or rotate along a fixed axis in space. Designing large stroke flexures that are not limited by these effects can be complex due to the low number of available design tools and examples to guide engineers. In addition, this design difficulty can be worsened by nonlinearities that occur with large deformations which complicate stress and stiffness analysis [2, 8].

However, recent studies have renewed insight in the design of flexure mechanisms for large stroke

applications. Multiple studies show, for example, different compliant rotational and spherical joints capable of deflecting at angles greater than ±25° without violating stress limits or considerably losing support stiffness [9–12]. The performance of various systems designed by Sioux Technologies can significantly benefit from the use of large stroke compliant joints. Due to the demand for increasingly accurate mechanisms, it is essential for Sioux Technologies to gain understanding of these type of joints.

1.2 Project description

This project was created by Sioux Technologies to obtain knowledge about large stroke compliant joints. More specifically, the main goals of this thesis are:

- to obtain a design method for large stroke compliant joints in accurate motion systems,
- to study critical and practical design aspects, and potential risks for implementing large stroke compliant joints in these systems.

To obtain, test, and demonstrate these aspects, a case study with challenging requirements was specified by Sioux Technologies. This case study involved designing a large stroke two degree of freedom (DoF) translation stage that is entirely guided by compliant joints. The function of this motion stage is to position a print head in a 3D print setup as will be described in Section 1.3. Because the translation stage design was used for theoretical studying proposes, the level of detail of this design had to be such that it presented a realistic concept in terms working principle, physical properties, materials used, strength, and stiffness. A design that was ready to be manufactured was not required. In addition, there was no need to pay attention to other components of the 3D print setup apart from the requirements specified by Sioux Technologies.

To achieve the goals of this thesis, a set of design requirements for the translation stage was first specified in accordance with Sioux Technologies. Thereafter, it was essential to obtain knowledge on designing compliant joints. An extensive literature study was done to find existing systems that include large stroke compliant joints to gain understanding in which properties are desired for their design and which are not. In addition, a literature study was done to find different types of large stroke compliant joints and to find existing design methods. A joint design method has been adopted from literature and applied to the design of the RR mechanism. Multiple critical design aspects and the potential risks have been found with designing the flexure-based translation stage.

1.3 3D print setup

Figure 1.2c illustrates the 3D print setup in which the flexure based translation stage must operate. The setup consists of a printhead, the xy-stage positioning the printhead in the horizontal translations (which is considered in this thesis), a print bed, and a z-stage that drives the print bed in the vertical direction. The print setup is based on the fused deposition modeling (FDM) 3D print method. With FDM printing, the printhead extrudes a melted thermoplastic material in a predefined path onto the print bed or a previously extruded layer. By building up multiple layers of material, this printing method can form a three dimensional part, as illustrated in Figure 1.2.
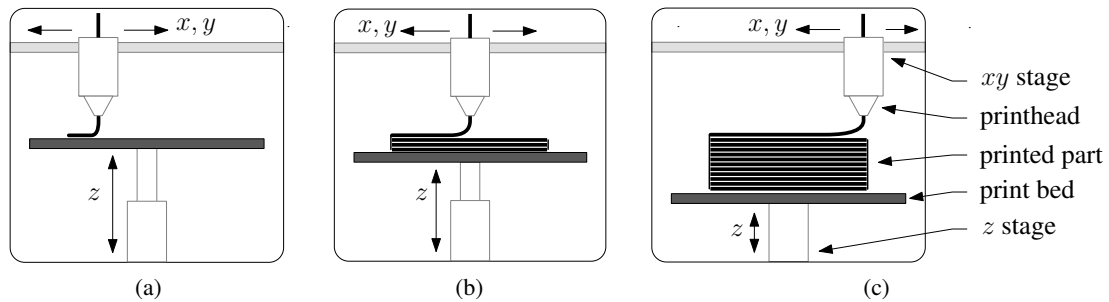
Figure 1.2: Schematic overview 3D print setup and printing process: (a) printing the first layer, (b) printing an intermediate layer, (c) printing the final layer and components of the setup

1.4 Thesis outline

In Chapter 2, the requirements for the flexure-based xy-stage are first discussed. Thereafter, the conceptual design of the motion stage and an overview of the final design is shown. In the next chapter, the design of the compliant joints is explained. First, a design method is described. Thereafter this design method is used for the joints of the translation stage designed in this thesis. Chapter 4 presents the design of the arms of the translation stage. Chapter 5 shows the design of the actuators driving the translation stage. In Chapter 6, the design of the measurement system is described which is used to measure the position of the end effector. Finally, some concluding remarks are given in Chapter 7.

2. Requirements and conceptual design

This chapter first discusses the design requirements for the flexure based translation stage. Thereafter, a conceptual design is proposed for this system. Finally, an overview is shown of the design that resulted from this thesis to provide a clear understanding of components discussed in the following chapters.

2.1 Requirements

The requirements for the flexure-based two DoF translation stage have been determined from discussions with the customer of this project [13]. This section first describes multiple general design requirements such as functionality and system dimensions. Thereafter, various motion requirements (e.g. accuracy, speed) and stability and environment requirements (e.g. transport temperature range) are listed.

2.1.1 General design

The function of the translation stage is to accurately position a printhead in two horizontal translations (x and y). The printhead has not yet been designed; therefore, it is considered as a box with a mass of 0.5 kg. The dimensions of this box and the position of its center of mass (CoM) are given in Figure 2.1.
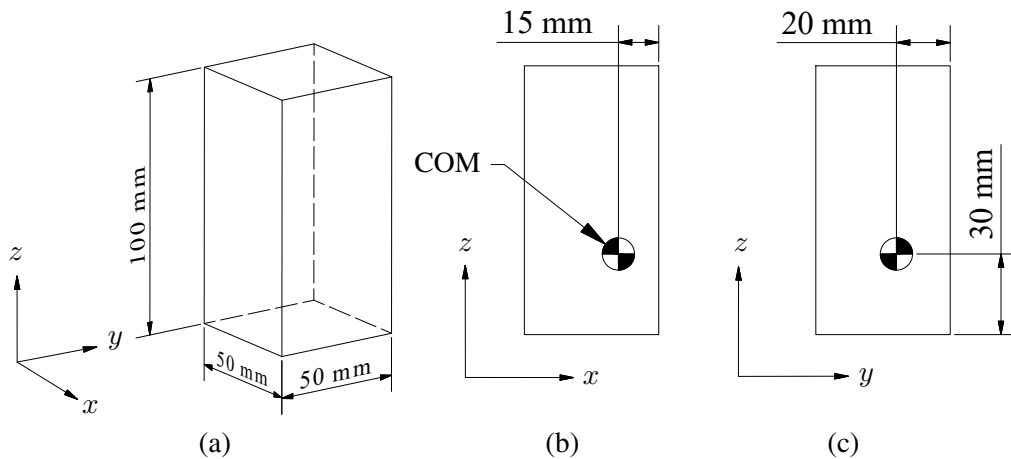
Figure 2.1: End effector dimensions and CoM position (unit: mm); (a) isometric view, (b) front view, (c) right view.

The 3D print setup must be able to operate on a desk which limits its maximum dimensions. The requirements set for these dimensions are shown in Figure 2.2. The maximum space in which the
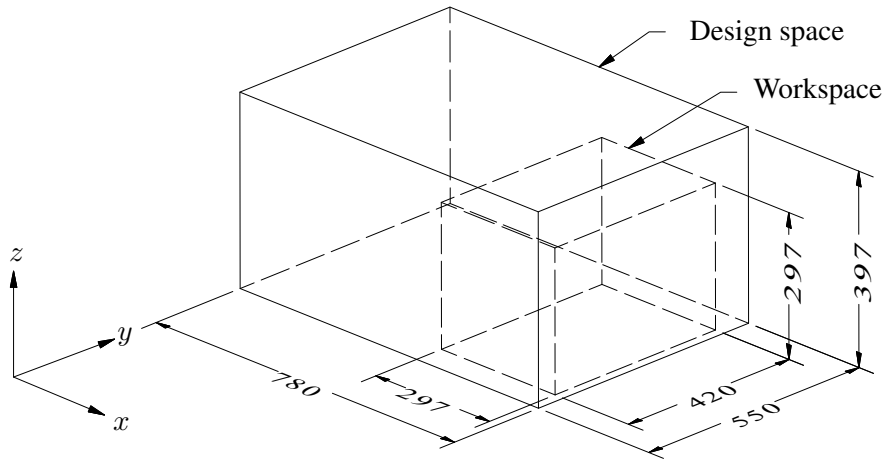
Figure 2.2: Maximum system dimensions and workspace dimensions

translation stage may operate is indicated in Figure 2.2 as the 'design space'. In this same figure, the minimum volume that the 3D print setup must be able to print is denoted as the 'workspace'. The workspace lies inside of the design space, its position and orientation in the horizontal plane are not constrained within this design space. Components of the translation stage may never enter the workspace volume to avoid collision with printed parts. The previously mentioned requirements and other general design requirements are summarized in Table 2.1.

Table 2.1: General design requirements

ID	Parameter
1	The mechanism has at minimum two translational DoFs: x and y.
2	Only compliant joints may be used for guidance.
3	The motion stage should be able to carry the 0.5 kg printhead specified in Figure 2.1.
4	The minimum workspace dimensions are 297×420×297 mm (x, y, z).
5	The maximum design space dimensions are 780×550×397 mm (x, y, z).
6	The xy-stage may not intersect with the workspace.

2.1.2 Motion

For the 3D print setup, two types of motions are considered – travel motion, where no printing is performed, and printing motion. During printing, a certain level of position accuracy of the translation stage is desired to ensure quality of the printed parts. If the printhead must move from one spot to another without printing, lower accuracy is required; however, higher speed and acceleration is preferred to minimize processing times. If the stage is not powered, the operator must be able to move the printhead by hand to remove printed parts from the print bed. The requirements associated with these aspects are summarized in Table 2.2.

Table 2.2: Motion requirements

ID	Parameter	during printing	during travel	Unit
7	Minimum position accuracy (x, y, z)	50	100	µm
8	Minimum velocity (x, y)	0.25	0.5	m/s
9	Minimum acceleration (x, y)	5	10	m/s^2
10	Minimum jerk (x, y)	100	200	m/s^3
11	The print head should be movable by hand when the stage is not powered.			-

2.1.3 Stability and environment

To ensure quality of the designed mechanism, various stability and environment requirements have been specified. These requirements are listed in Table 2.3.

Table 2.3: Stability and environment requirements

ID	Parameter
12	The mechanism must be able to travel 26 280 km without breaking.
13	A force of no more than 1 N must not increase position uncertainty in the x and y direction.
14	A force of no more than 0.1 N must not increase position uncertainty in the z direction.
15	The maximum position uncertainty requirements must be met in the temperature range of 15 °C to 32 °C.
16	The mechanism must not damage during transport within the temperature range from −25 to 55 °C.

2.2 Principle concept translation stage

Multiple conceptual layouts have been evaluated for the flexure based xy stage in order to meet the requirements listed above. The considerations that have been made for these layouts are as follows:

1. For dynamic performance, it is essential that the mechanism has high stiffness and has a low moving mass and inertia [4].
2. A design with few components is preferred to minimize position errors from manufacturing and assembly tolerances.
3. For the 3D print setup, a minimum number of DoFs necessary for printing (x, y, and z) is desired. Redundant DoFs require additional actuators and sensors that can increase position errors and control complexity. As stated in the requirements, the x and y DoF must be incorporated in the motion stage. The z DoF may be integrated if this is favorable.
4. Preferably, the position accuracy of the mechanism is insensitive to thermal expansions.

When concepts were created for the xy stage, a distinction was made between parallel and serial layouts because they have several distinct characteristics. Parallel mechanisms are defined as arrangements of at least two kinematic chains connecting the fixed world to a single platform, some

examples of which are shown in Figure 2.3. Furthermore, serial mechanisms consist of conjugated single or multi DoF mechanisms [14]. A key advantage of parallel mechanisms is that the actuators can often be mounted to the fixed world, which results in a low moving mass. In addition, the stiffness of all kinematic chains contribute to the overall stiffness of the supported platform, in contrast to serial mechanisms. Unfortunately, no concept has been found that meets the minimum workspace and maximum footprint dimensions due to the limited deflection angles of the compliant joints. Within the limited space considered here, serial layouts can most likely achieve greater operating ranges than parallel mechanisms. Thus, making them preferred.
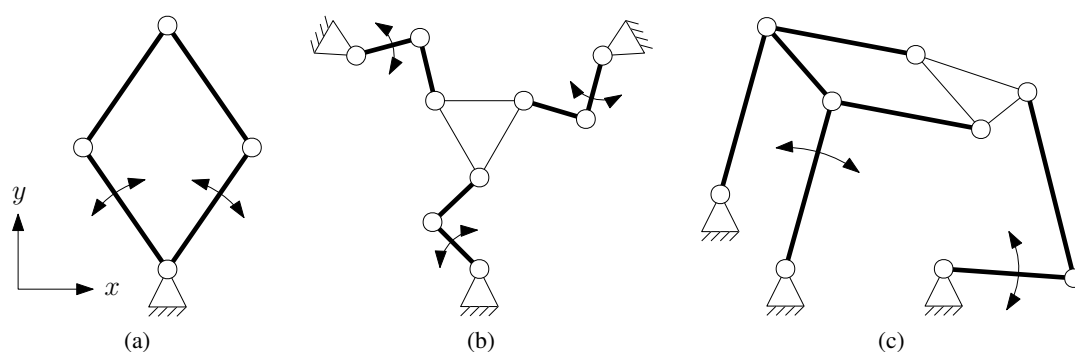
Figure 2.3: Parallel xy stage concepts (top views); (a) double RR mechanism, (b) triple RRR mechanism, (c) Drafting machine mechanism with actuation link.

Two kinds of serial layouts have been considered – spatial and planar. With planar mechanisms, all joints and links move in parallel planes and with spatial mechanisms these components move in 3D space. Evaluation of multiple concepts showed that spatial mechanisms often suffer from parasitic vertical motions, an example of which is illustrated in Figure 2.4. This vertical motion depends on the kinematic configuration and on the parasitic motions of the compliant joints. Part of the vertical motion can be resolved by using a configuration that produces a continuous vertical output or by incorporating the z DoF in the motion stage. However, these solutions typically result in a high part count or a high moving mass. Planar xy mechanisms do not suffer from this inherent parasitic vertical motion and therefore were found to be best suited for this application.

Of all evaluated planar concepts, only one was found that meets the workspace requirements if it were to be designed with dimensionless components and a maximum joint angle of $\pm 30°$. Figure 2.5 shows this so-called RR mechanism, which consists of two arms connected in series and two actuated rotational joints. Although this mechanism is not as ideal in terms of stiffness and moving mass compared to parallel structures, it can achieve large displacements with few components. Therefore, this concept has been selected. For other evaluated concepts, see Appendix A.

The names used in this thesis to describe components of the RR mechanism are as follows: the joint connected to the fixed world is denoted by joint 1, the other by joint 2. Similarly, the link connected to joint 1 is denoted as arm 1, the other as arm 2.
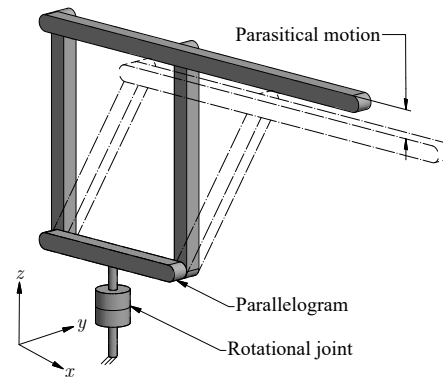
Figure 2.4: Polar coordinate spatial two DoF mechanism with parasitic vertical motion. The shaded and overlay view illustrate two different configurations of the mechanism.

Symbol	Parameter
l_1	Length Arm 1
l_2	Length Arm 2
s_x	x stroke
s_y	y stroke
W_x	Workspace center x coordinate
W_y	Workspace center y coordinate
θ_1	Angle arm 1 w.r.t. the x axis
θ_2	Angle arm 2 w.r.t. arm 1
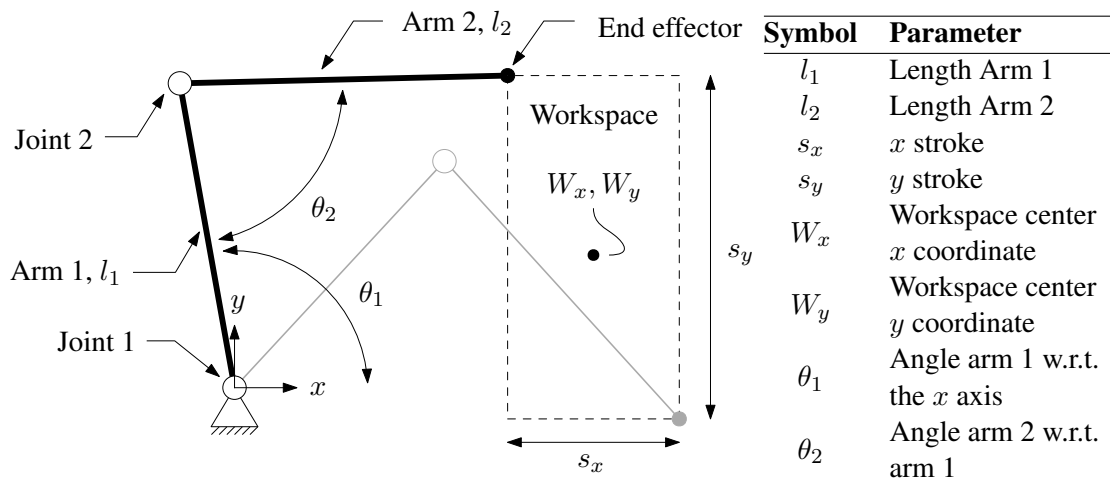
Figure 2.5: A top view of two configuration of the RR mechanism layout (black and gray lines) and associated parameters.

2.2.1 Optimization layout parameters

Finding a set of parameters for the RR mechanism such that it meets the requirements of the workspace and footprint dimensions is cumbersome to achieve analytically. Therefore, an optimization algorithm in combination with a parametric kinematic model has been used to find these parameters. Unfortunately, no feasible solution was found when the actual dimensions of components (e.g. joints and arms) were taken into account. As an alternative, Sioux Technologies agreed to set the optimization goal to maximize the rectangular workspace area within the initially specified footprint dimensions. The resulting design parameters are listed in Table 2.4, which achieves a workspace area that is 14% smaller than initially required. However, when neglecting the maximum outer dimensions, the total workspace area of the RR mechanism is about 1.5 times larger than initially required. Details about this optimization, the kinematic model, and the results

are described in Appendix B.

Table 2.4: RR mechanism design parameters

Parameter	Symbol	Value	Unit
Length arm 1	l_1	420	mm
Length arm 2	l_2	476	mm
Center x coordinate workspace	W_x	431	mm
Center y coordinate workspace	W_y	180	mm
Stroke in the x direction	s_x	224	mm
Stroke in the y direction	s_y	480	mm
Maximum joint angle	$\theta_{\max}$	± 30	°

2.3 Design overview

To provide a clear understanding of components discussed in the following chapters, the design of the translation stage that resulted from this thesis is summarized here. Figure 2.7 shows an exploded view of the flexure-based RR mechanism and shows the names of all components. In addition, Figure 2.6 shows this mechanism in two extreme configurations. As explained in Section 2.2, the mechanism consists of two arms and two compliant joints. The arms are sheet metal structures made from EN AW-6082 T6 aluminum. The selected types of joints are called 'infinity hinges' and they are made from Stavax stainless steel. Each arm is driven by a linear ironless motor. These motors consist of a coil unit and an arc-shaped magnet yoke. The magnet yoke used to drive arm 1 is fixed to the world, the magnet yoke used to drive arm 2 is fixed to arm 1. To determine the position of the end-effector (the printhead), two linear magnetic encoders are used. Each encoder consist of a read head and an encoder scale.

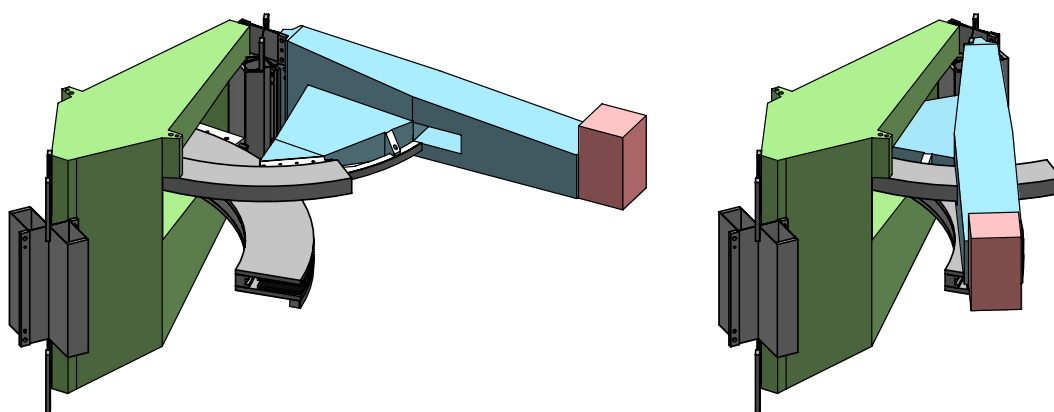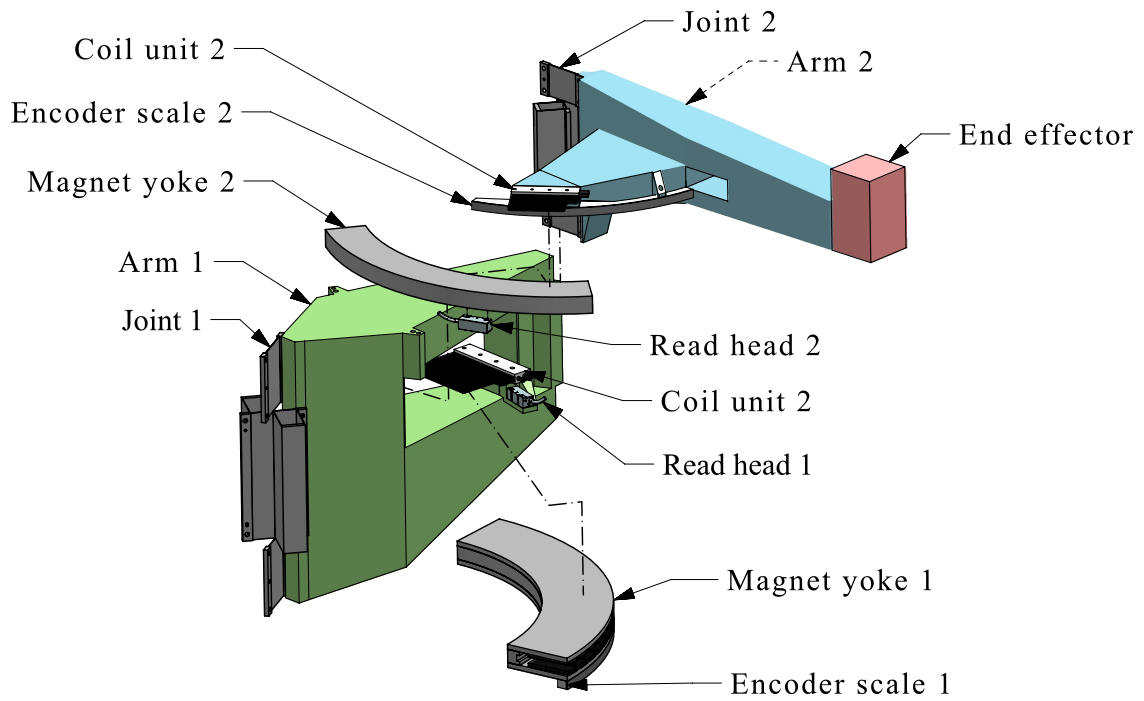Figure 2.6: Overview RR mechanism in two configurations

Coil unit 2

Encoder scale 2

Magnet yoke 2

Arm 1

Joint 1

Joint 2

Arm 2

End effector

Read head 2

Coil unit 2

Read head 1

Magnet yoke 1

Encoder scale 1

Figure 2.7: Final RR mechanism design (exploded view)

3. Compliant joint design

In this chapter, a design method is obtained for compliant joints and joints are designed for the RR mechanism. The reason why the joint designs are presented first is to show the origin of considerations made for other components of the RR mechanism, that are discussed in the next chapters. In the first section, important properties are described for the evaluation of compliant joints. A key finding from this section was that optimization algorithms can help with making a fair comparison between different types of joints. Therefore, the subsequent section describes a performance optimization method for compliant joints. Next, these evaluation and optimization methods are used in the design of the joints for the RR mechanism. Finally, some concluding remarks are given.

3.1 Method for evaluating compliant joints

When considering multiple types of compliant joints for a particular accurate motion system, it is important to note which aspects are most critical for the evaluation of these joints: first, the joint must be manufacturable to be implemented in a physical system. Second, internal stresses must be limited such that the joint is be able to carry its load without breaking and such that no plastic deformation occurs. Next, for some applications the parasitical motions must be limited. Furthermore, a low required actuation force or torque is desired to minimize actuation effort. Finally, for high position accuracy it is essential to have great stiffness in the supporting (constrained) DoFs.

The importance of supporting stiffnesses with respect to the performance of the joint depend on the load connected to it. To give an example: for a load with high translational inertia, high translational stiffness is important. In contrast, for a load with high rotational inertia, high rotational stiffness is important. The measure that shows the importance of stiffnesses for a given load is the first unwanted eigenfrequency [1], which is preferably as high as possible. For single DoF compliant joints, this value is typically given by the second eigenfrequency. The first eigenmode is caused by compliance in the free DoF, which will typically be supporter by an actuator. Note that compliant joints typically lose support stiffness when deflected. Hence, the first unwanted eigenfrequency is given by the lowest second eigenfrequency across the joint's motion range.

The measure for comparing the performance of different compliant joints is thus the first unwanted eigenfrequency. However, this value can significantly vary for a single joint type, given different geometry parameters (e.g. length, thickness, height). To make a fair comparison between different types of joints, their geometries must be optimized with respect to their first unwanted eigenfrequencies, given the load for which it is used. An added benefit of this optimization is, obviously, that it provides the ideal performance for a given application.

In summary, compliant joints for accurate positioning systems should be compared as follows:

---

[1]An eigenfrequency that can disturb the position accuracy of the end effector when it is excited.

1. Select different kinds of compliant joints.
2. Optimize their geometries with respect to their first unwanted eigenfrequencies, given the load for which it is used. In this step, take into account manufacturability, maximum allowable parasitical motions (if required), minimum strength, and other relevant constraints.
3. The joint with the highest first unwanted eigenfrequency is considered to be the best in terms of performance.

3.2 Joint performance optimization method

In this section, a description is given of the performance optimization method used for designing and comparing compliant joints. The method described here primarily focuses on the design of the RR mechanism designed in this thesis, which exceptionally uses single DoF rotational joints. However, the method can easily be extended for use on other mechanisms.

3.2.1 General description

The goal of the optimization is to maximize the first unwanted eigenfrequency of a compliant joint with a given load attached to it. As explained in Section 3.1, this value is typically given by the lowest second eigenfrequency across the motion range of the joint. The optimization method considered here has been adopted from [6]. This method uses an optimization algorithm in combination with finite element method (FEM) software to tune the parameters that describe the geometry of the considered joint (e.g. length, width, height). To ensure the optimization algorithm produces a feasible design, constraints are specified such as maximum stress and maximum dimensions of components. In summary, the optimization method works as follows:

1. A load case is defined to which the joint will be subjected.
2. A set of parameters is selected that describes the geometry of the considered joint.
3. Constraints are defined that solutions returned by the optimization algorithm must satisfy.
4. An optimization algorithm searches for a set of optimal parameters using a FEM program.

The load case, the constraints, the optimization method, and the FEM software used in this thesis are summarized in the following subsections. A more detailed description of these aspects is given in Appendix D. Examples of geometry parameters and optimization results are shown in Section 3.3.

3.2.2 Load case

In general, a load case is given by the following parameters:

- a mass m,
- an inertia tensor $\underline{J}$ derived from the CoM,
- a vector describing the position of the load's CoM $\underline{r}_{COM}$.
- the gravitational constant $g = 9.81$ m/s^2,
- the parameter ϕ that describes the orientation of the load with respect to the joint.

The reference frame from which these properties are derived is such that the joint's initial axis of rotation aligns with the vertical (z) axis, and the xy plane aligns with geometric center of the joint, see Figure 3.1. The parameter ϕ is used to rotate the load about with respect to this reference frame for optimal alignment with the joint. Note that ϕ rotates the load about the rotation axis of the joint.

(a)

(b)
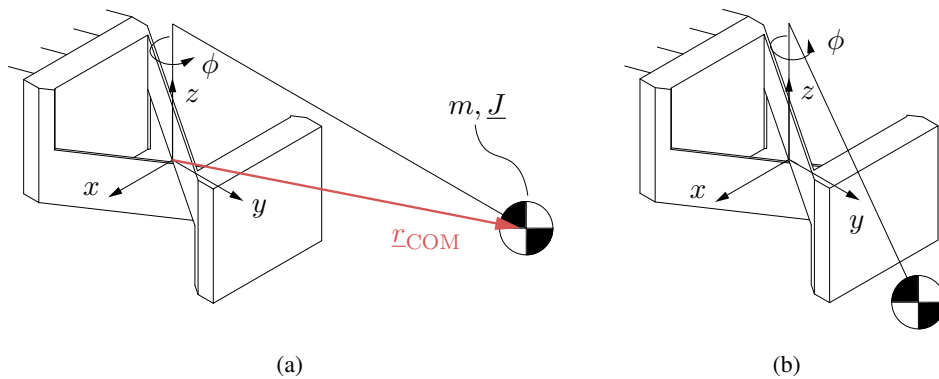
Figure 3.1: Visualization load parameters: (a) initial position of the load with respect to the joint, (b) load rotated with about the z axis with parameter ϕ.

The load cases for joint 1 and 2 of the RR mechanism have a critical difference. For joint 2, the load parameters are fixed with respect to the moving part of the joint over the entire motion range. However, for joint 1, the position of the CoM and the size of the inertias depend on the parameter θ_2, as illustrated in Figure 3.2. Note that this load is not dependent on the orientation of Arm 1 as the load is fixed to the rotating part of the joints. To be able to optimize joint 1 over the operating range of the RR mechanism, this varying load has been taken into account. For details about how
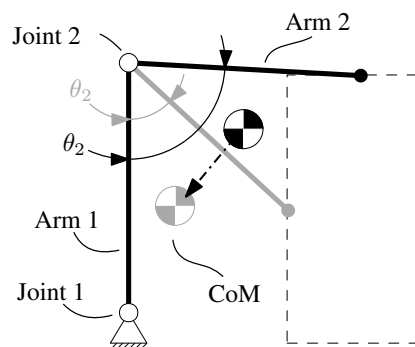
Figure 3.2: Dependency position of the CoM on parameter θ_2

the load parameters are rotated using parameter ϕ and how the load parameters are computed for joint 1, see Appendix D.

3.2.3 Constraints

The constraints specified for optimization are as follows: the joints may have a maximum stress of $\max(\sigma) \leq \sigma_{\max}$, which follow from the joint's material properties. Furthermore, a maximum actuation torque $\max(M) \leq M_{\max}$ has been set to limit actuation forces. To ensure manufacturability, a maximum height for components manufactured by wire EDM has been set to $h_{\max}$ and a minimum thickness of $t_{\min}$. Different joints may require unique constraints, examples of which are given in Section 3.3.1. The values of these constraints for the joints of the RR mechanism are given in Section 3.3.4.

3.2.4 Optimization

Most optimization algorithms aim at finding a set of variables $\boldsymbol{p}$ for which an objective function $\mathcal{F}(\boldsymbol{p})$ is as small as possible. For this optimization problem, the set $\boldsymbol{p}$ is defined by the geometry parameters of the considered joint. Because the goal is to maximize the lowest second eigenfrequency across the operating range of the joint, the objective function is defined as the inverse of this value

$$\mathcal{F}(\boldsymbol{p}) = \min_{Q} \left(f_2(\boldsymbol{p}, Q)^{-1} \right) \forall Q, \tag{3.1}$$

where Q defines the operating range of the joint. For joint 2, this parameter is given by all feasible joint angles $Q = \{\theta_{2,\min} \quad \ldots \quad \theta_{2,\max}\}$. For joint 1, Q is defined by all configurations of the joint and RR mechanism (the load) where the end effector lies inside of the workspace:

$$W_x - s_x/2 \leq x \leq W_x + s_x/2$$
$$W_y - s_y/2 \leq y \leq W_y + s_y/2$$

Where x and y denote the end effector position. Furthermore, a set of constraints is defined according to Section 3.2.3

$$\mathcal{C}(\boldsymbol{p}) = \begin{Bmatrix} \max_{Q}(\sigma(\boldsymbol{p}, Q)) - \sigma_{\max} \\ \max_{Q}(M(\boldsymbol{p}, Q)) - M_{\max} \\ h - h_{\max} \\ t_{\min} - t \end{Bmatrix},$$

for which any solution must comply to $\mathcal{C}(\boldsymbol{P}) \leq 0$. This defines the optimization problem as

$$\boldsymbol{p}_{opt} = \arg \min_{\boldsymbol{p}} \mathcal{F}(\boldsymbol{p}) \text{ subject to } \mathcal{C}(\boldsymbol{p}) \leq 0.$$

Multiple parameters used in this optimization problem are obtained using FEM software, which means that their derivatives with respect to the variables p are difficult to obtain. Therefore, a derivative free optimization algorithm is desired. In addition, this algorithm must be able to solve nonlinear problems as the objective and constraint functions include nonlinearities (such as the maximum stress). The selected algorithm is a Nelder-Mead based solver [15] that has been modified to include constraints. The primary reason for this selection is its efficiency. Other algorithms have also been tested, which gave comparable results. The optimization problem was evaluated in MATLAB®. More details about this optimization are described in Appendix D.

3.2.5 Modeling

To obtain the eigenfrequencies and constraint parameters, the SPACAR FEM software [16] has been used. This software uses simplified nonlinear beams to simulate mechanical properties of flexible systems. The major advantage of this software with respect to other FEM programs is that it typically runs simulations several orders of magnitude faster, which is desirable when performing many iterations during optimization. The SPACAR models include transverse shear and torsion-extension coupling [16]. The effect of torsion-stiffening is added to the models using the method described in [6].

3.3 Joint design for the RR mechanism

This section describes the design of the joints of the RR mechanism that have been obtained using the methods described earlier this chapter. First, multiple types of joints are described that have been considered for the RR mechanism. Next, a material is selected for these joints. Finally, the optimization input parameters are derived, different joints are evaluated and the resulting joints are presented.

3.3.1 Joint topologies

Multiple kinds of large stroke compliant joints have been found in literature that have great potential for accurate motion systems. The joints that have been selected to evaluate here were chosen for the following reasons:

- The design was assumed to be feasible in terms of manufacturability, strength, and stiffness.
- Sufficient information could be found to implement the considered design in SPACAR and MATLAB$^{®}$.
- Evaluating the design was expected to be possible within the time span of this project.

Figure 3.3 shows the joints that have been evaluated. Other joint concepts are described in Appendix E, some of which are highly recommended to further investigate. In the following part of this subsection, descriptions and the geometry parameters of the different joints are discussed. For the design parameters, note that the height parameter H is fixed in optimization and therefore is not a variable.

Cartwheel hinge

Figure 3.3a shows the design of the cartwheel hinge (CWH) [17]. This joint consists of four equal plate springs that all connect to the geometric center of the joint, which is also the initial center of rotation. The height H has been fixed to the constraint value $h_{\max} = 160$ mm and all flexures have the same thickness t. The optimization variable set $\boldsymbol{p}$ that describes the CWH geometry is defined by

$$\boldsymbol{p} = \begin{bmatrix} l & w & t & \phi \end{bmatrix},$$

where l and w describe the length and width respectively. Note that ϕ denotes the orientation of the load as described in Section 3.2.

(a) Carthweel hinge (b) Three flexure cross hinge (c) Five flexure cross hinge

(d) Modified infinity hinge (isometric view) (e) Modified infinity hinge (front view)
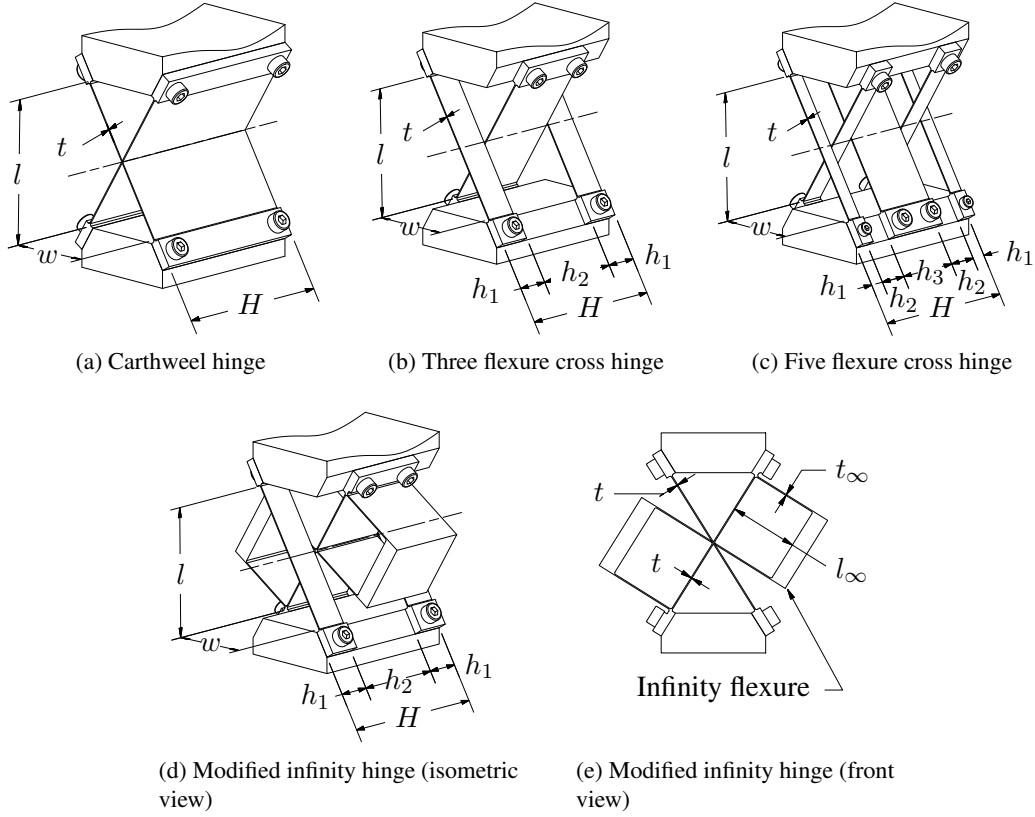
Figure 3.3: Evaluated compliant joints and associated design parameters

Three flexure cross hinge

The three flexure cross hinge (TFCH) shown in Figure 3.3b is the generally stiffer successor of the cross spring pivot [1, 4]. This design is composed of three plate springs that cross each other in the center of the plates. All flexures have the same thickness t. The parameters describing the geometry of the joint are given by:

$$\boldsymbol{p} = \begin{bmatrix} l & w & t & h_1 & \phi \end{bmatrix},$$

where h_1 describes the height of the outer flexures. The height of the inner flexure h_2 is calculated as:

$$h_2 = H - 2h_1. \tag{3.2}$$

3.3.2 Five flexure cross hinge

The five flexure cross hinge (FFCH) is a derivative of the TFCH which includes two more flexures, as shown in Figure 3.3c. The outer flexures are equal to each other, as well as both flexures with height h_2. In addition, all flexures share the same thickness t. The parameter set describing the

geometry of the joint is given by:

$$\boldsymbol{p} = \begin{bmatrix} l & w & t & h_1 & h_3 & \phi \end{bmatrix},$$

where h_1 and h_3 describe the height of the outer and inner flexures respectively. The height h_2 is calculated as:

$$h_2 = (H - 2h_1 - h_3)/2.$$

Infinity hinge

The infinity hinge (INFH), shown in Figure 3.3d and 3.3e is a patented design [18] that includes a torsionally stiffened plate spring, see in Figure the 'Infinity flexure'. This plate spring has two 'parallelograms' placed laterally to it such that it becomes stiff in its longitudinal direction, but a rotational DoF remains free. The design shown in Figure 3.3 is a modified version of the original infinity hinge described in [6]. The design considered here has two plate springs on the outer side of of the joint, where as the initial design does not have these plate springs but a single wire flexure that runs through the infinity flexure. This modification was made to obtain more height and thus more stiffness. The parameter set describing the geometry of the joint is given by

$$\boldsymbol{p} = \begin{bmatrix} l & l_\infty & w & t & t_\infty & h_1 & \phi \end{bmatrix},$$

where l_∞ and t_∞ denote the length and the thickness of the infinity flexure. Furthermore, h_1 denotes the height of the outer flexures and the height of the infinity flexure h_2 is computed with (3.2).

The 'parallelograms' of the infinity hinge both have an internal DoF. This DoF may not have to be disadvantageous for performance, as these DoF move in the direction that can be supported by the actuators of the RR mechanism. To minimize the risk that the optimization algorithm tries to increase this eigenfrequency instead of a more critical eigenfrequency, the intermediate bodies of the parallelograms are modeled to be massless and rigid.

3.3.3 Material selection

A concise analysis was done to obtain a feasible material for the compliant joints. Three aspects have been taken into account for the material selection:

1. The material must be strong enough to withstand the cyclic loads from operation and flexible enough to attain elastic deformation. Thus, a high fatigue strength to Young's modulus ratio $R = \sigma_\mathrm{f}/E$ is preferred [2].
2. A fabrication method must exist to process the material into the desired shape.
3. A material is desired that does not suffer from creep at the transport temperature range of -25 to $55\,^\circ\mathrm{C}$ (see requirements, Section 2.1.3).

Considering these aspects, metals are expected to be highly suitable. Numerous strong but flexible metals exist that can be machined with sufficient accuracy and which generally do not creep at the temperature range considered here.

To compare the fatigue strength of different metals, the number of load cycles had to be known. This value was estimated by dividing the minimum required operating distance without failure (see requirements) by the circumference of the workspace area, which gives

$$\frac{26280 \cdot 10^3}{2 \cdot 0.480 + 2 \cdot 0.224} \approx 18.7 \cdot 10^6 \text{ load cycles.}$$

Table 3.1 lists several alloys that have been considered as they are often used in compliant joints. As can be seen from this table, the titanium Ti 6Al 4V alloy performs the best in terms of the ratio R. However, tests done by Sioux Technologies show that this alloy generally does not perform as well as stated in various sources [19]. The fatigue strength of Ti6Al4V can degenerate due to EDM, which might be the reason for this lower performance [20]. Stavax is a better alternative to Ti 6Al 4V according to these tests, which has therefore been selected.

Material	R_m [MPa]	σ_f [MPa]	E [GPa]	G [GPa]	ρ [kg/m^3]	$R \cdot 10^3$ [-]	Reference
Ti 6Al 4V (grade 5)	1100	510	110	40	4400	4.6	[21]
Stavax	1780	623[*]	200	80	7800	3.1	[22]
AISI 301	1207	422[*]	193	70	7880	2.2	[23]

Table 3.1: Materials considered for the compliant joints and corresponding mechanical properties. R_m is the ultimate tensile strength, G is the shear modulus, and ρ is the mass density. Fatigue strength properties marked by [*] have been estimated as $0.35 \cdot R_m$ according to [24].

3.3.4 Optimization input parameters

The load parameters (masses, inertias, CoM position vectors) used for optimization have been obtained from CAD models of the RR mechanism. The values of these parameters given in Appendix H.

The constraints specified for optimization are as follows: the joints may have a maximum stress of $\max(\sigma) \leq \sigma_{\max} = 620\,\text{MPa}$, following from the material properties described in Section 3.3.3. Furthermore, the maximum actuation torque $M_{\max}$ has been set to 9 N m for joint 1 and 5 N m for joint 2. These values have been selected such that the actuators designed in Chapter 5 are not overloaded during operation. The maximum plate spring height has been set to $h_{\max} = 160\,\text{mm}$ and the minimum thickness $t_{\min} = 0.2\,\text{mm}$, as this is considered to be manufacturable with sufficient accuracy [19]. The height H of joint 1 has been specified as 320 mm, as this was considered as manufacturable. Furthermore, the height H of joint 2 has been set to 200 mm. Initially, this height was set to 100 mm such that this joint could fit above the workspace, which is advantageous for the size of this workspace. However, the optimization algorithm did not return any feasible solutions with this constraint and therefore this height was increased. The selected height of 200 mm was practically to implement to arm 2 and provided provided feasible results from optimization. Finally, a constraint has been defined that only applies to the infinity hinge optimized for joint 2. The parallelograms of the infinity flexure intersect with arm 1 when mounted to this arm. To be able to design a feasible design of this arm, the maximum height of the inner flexure h_2 has been set to 120 mm.

3.3.5 Results

The parameters of the different joints returned by optimization are listed in Table 3.2. As can be seen in this table, the infinity hinge performed the best for both joints of the RR mechanism in terms of the worst case second eigenfrequency. All results were limited by the maximum stress and actuation moment constraints, which shows how essential these factors are for performance of the joint. Figure 3.4 relates the performance of topologies optimized for joint 1 to the position of the end effector of the RR mechanism. As can be seen in this figure, the TFCH and FFCH have higher initial eigenfrequencies, but their performance decreases rapidly. In addition, the infinity hinge shows to have a 'ceiling' for the higher eigenfrequencies. This ceiling is caused by the internal DoFs, which are dominant when the joint is not deflected. Furthermore, Figure 3.5 plots the eigenfrequencies for the optimized flexures for the second joint of the RR mechanism. Similar to the results from joint 1, the infinity hinge does not have the highest eigenfrequency. This is most likely caused by the additional constraint limit of 120 mm of the center flexure, which the other joint types do not have. In summary, the infinity hinge has the highest worst case eigenfrequencies for both joints of the RR mechanism. Although it does not have the highest eigenfrequency in its undeflected state, its performance is more stable compared to the other joints. Therefore, this joint type has been selected for both joints of the RR mechanism. Figure 3.6 shows the resulting design.

Table 3.2: Optimal geometry and corresponding performance parameters. Parameters marked in red are limited by constraints.

| Parameter	Unit	CWH		TFCH		FFCH		INFH	
Joint	-	1	2	1	2	1	2	1	2
l	mm	310.2	177.1	54.6	48.1	54.6	52.0	46.6	44.5
l_∞	mm							45.8	38.0
w	mm	147.7	71.1	31.9	25.2	32.9	29.2	27.8	16.1
t	mm	0.65	0.44	0.58	0.53	0.58	0.55	0.50	0.43
t_∞	mm							0.42	0.41
h_1	mm	160.0	160.0	81.7	20.0	22.6	2.8	81.8	40.0
h_2	mm			156.6	160.0	58.0	17.8	156.3	120
h_3	mm					158.8	158.8		
ϕ	°	-0.3	3.0	-16.9	-3.5	9.8	-7.3	-5.4	-5.1
$\min(f_2)$	Hz	11.4	36.3	32.5	49.8	46.6	47.4	68.8	95.3
$\max(f_2)$	Hz	75.3	172.1	277.5	63.6	361.5	354.3	245.3	256.9
$\max(\sigma)$	MPa	620	620	620	620	620	620	620	620
$\max(M)$	N m	9	5	9	5	9	5	9	5
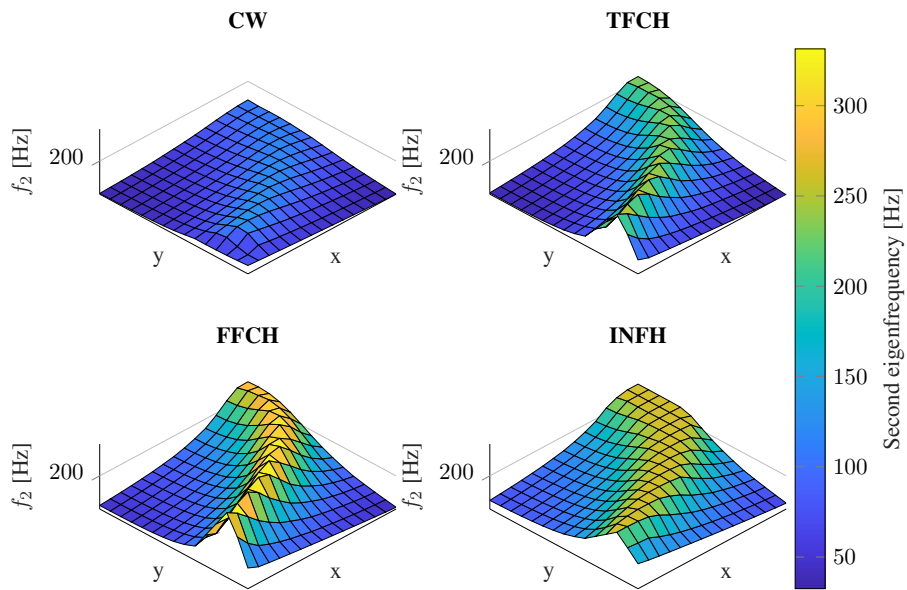
Figure 3.4: Eigenfrequencies of topologies optimized for joint 1 plotted across the workspace RR mechanism. Data is interpolated from SPACAR simulations.
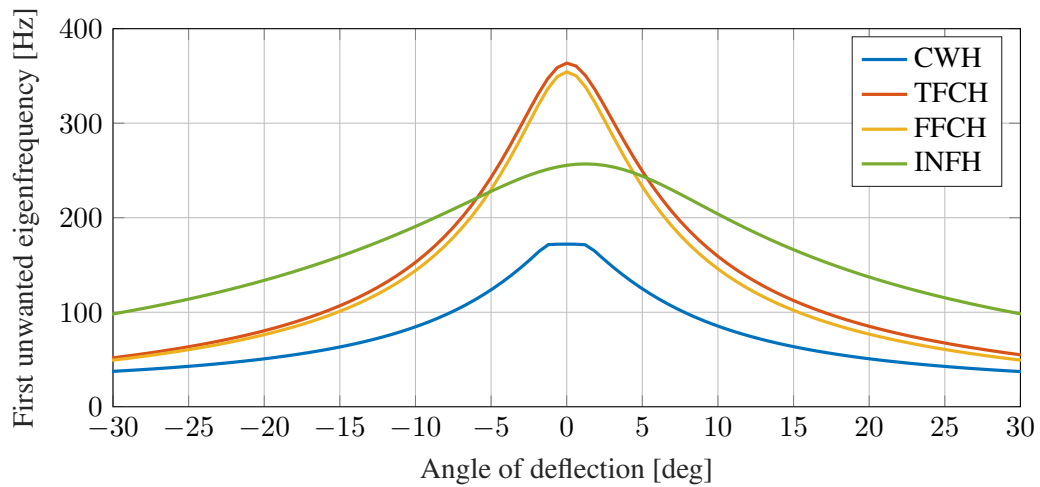

Figure 3.5: Eigenfrequencies of topologies optimized for joint 2 plotted across the operating range. Data is obtained using SPACAR.
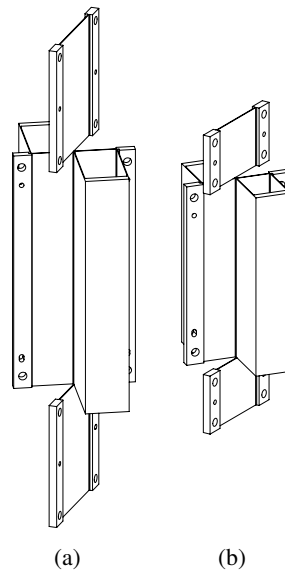
(a)   (b)

Figure 3.6: Infinity hinges RR mechanism: (a) joint 1, (b) joint 2.

3.4 Conclusions and recommendations

3.4.1 Conclusion

In this chapter, a design method for compliant joints was obtained. This method evaluates different compliant joints based on their first unwanted eigenfrequencies, as this is an essential performance parameter for these joints. To make a fair comparison between different kinds of joints and to obtain high performance, an optimization algorithm has been used to tune the geometry parameters of the joints. With this method, different joints have been compared for the RR mechanism. The resulting concept for both joints of the RR mechanism is the infinity hinge concept.

3.4.2 Recommendations

Alternative infinity hinge design

The parallelograms of the infinity flexures showed to have an internal DoF. If these DoFs turn out to be undesired, an alternative design from [6] of the infinity flexure can be studied that may not or suffer less from this problem. This design is shown in 3.7. The difference from this design with original infinity hinge is that the flexures that provide torsional stiffness are directly connected to each other, rather than by an intermediate body.
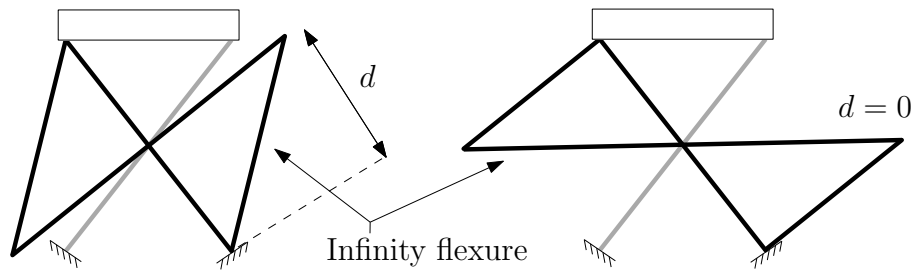
Figure 3.7: Two variations of the alternative INFH design from [6].

Validation

The SPACAR software used for simulating the performance of the joints has proven to be accurate in multiple studies [6, 7, 11]. However, setting up this program for simulation is prone to programming errors and therefore it is strongly recommended to perform validations on the results using, for example, other FEM simulations or physical tests of the joints.

Effects of overconstrained design

Multiple joints that have been considered are statically indeterminate, meaning that they constrain at least one DoF multiple times. This aspect can decrease motion predictability, internal stresses, and can result in higher required manufacturing tolerances. Further research on these effects are therefore strongly recommended.

Enhancing fatigue life

Although no extensive research was done on the fatigue properties of the joints, it is an important aspect to ensure the quality of the designed mechanisms. Here, a few suggestions concerning fatigue are given that are strongly recommended for further investigation: first, it is essential to ensure a smooth surface finishing of the flexures as this has been proven to significantly improve fatigue life [25]. A manufacturing method such as wire EDM that provides this is therefore highly desired. In addition, surface defects can be minimized by, for example, (electro)polishing. Furthermore, a key feature in improving fatigue life is to yield compressive surface stress, as cracks causing fatigue only propagate under tension. Treatments such as shot peening can help achieving this. An interesting variation of this process might be stress peening. With this process, the surface is pre-stressed in tension before projecting the shot, which results in a higher compressive after treatment. Finally, heat treatments such as hardening can improve (fatigue) strength and should therefore also be investigated [26].
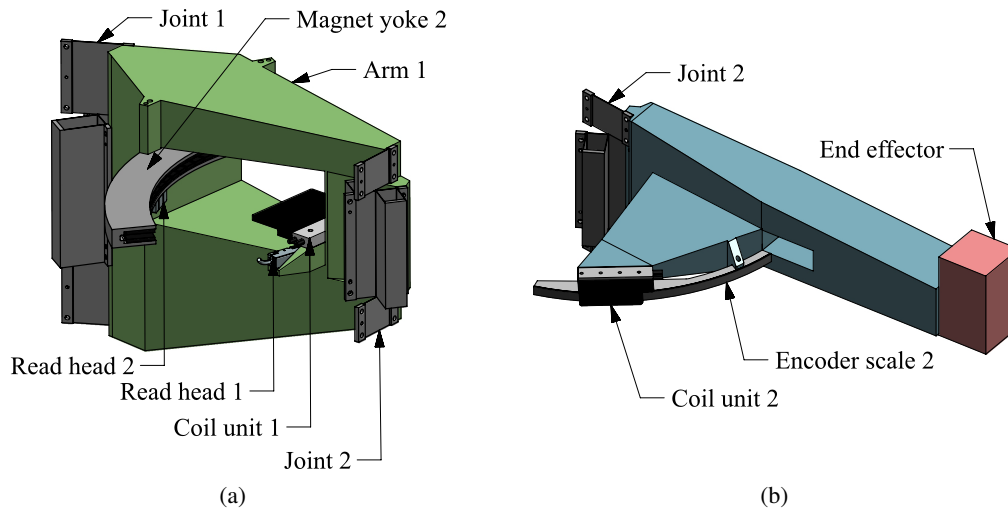
4. Arm design

Figure 4.1: Arm assemblies: (a) arm 1, (b) arm 2

The arms of the RR mechanism are used to support the end effector, to provide motion of this end effector, and to hold multiple actuator and sensor components. Figure 4.1 shows both arms of the RR mechanism and the components that are attached to it. This chapters discusses the design of these arms. In the first section, the design concepts and multiple design considerations discussed. Next, the detailed designs are presented. Finally, some concluding remarks are given.

4.1 Concept design and design considerations

The conceptual design of the arms started with the selection of the RR mechanism and the specified system requirements as described in Chapter 2. An optimization algorithm was used to maximize the workspace area of this concept, such that the maximum dimensions of the system were not violated and the arms and joints do not intersect with the workspace. Multiple iterations were done between the design of the arms, the joints, and the optimization algorithm. This process determined the arm lengths and it determined how the arms can be oriented with respect to each other.

For other dimensions and shapes of the arms, multiple considerations have been made. To minimize static and dynamic deflections, a stiff design was required. In addition, the mass of the arms needed to be low to minimize actuation forces and to minimize internal stresses of the joints. A balanced mass-stiffness ratio is desired to avoid unwanted vibrations of arms subjected to dynamic loads. As with the joints, this aspect translates in desirably high unwanted eigenfrequencies. To obtain high

23

stiffness and low mass, the outer cross sectional dimensions of the arms (e.g. height, width) have been made large and the wall thicknesses small. A sheet metal design was chosen for both arms to be able to create stiff and lightweight structures with custom shapes that fit the RR mechanism. The selected material for these structures is EN AW-6082 T6 aluminum due to its favorable specific stiffness E/ρ, weldability, and machinability. For initial concepts, steel was also considered as it can have a similar specific stiffness to aluminum. However, for aluminum and steel designs with the same amount of stiffness and mass, the steel design required too small wall thicknesses to be fabricated. Hence, aluminum was selected.

The concepts for the arms started with rectangular tubes, as shown in Figure 4.2. To obtain a high stiffness to mass ratio, components placed in series should contribute an equal amount of stiffness to the end effector [4]. This philosophy was used with selecting the cross sectional dimensions of the arms such that they contribute an equal amount of stiffness to the end effector as the joints.
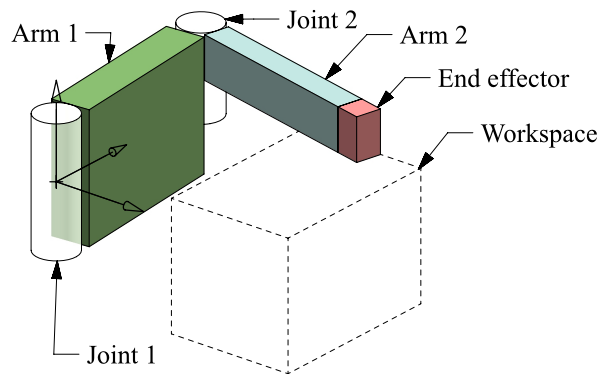

Figure 4.2: First concept of the arms

In a next design iteration, the linear actuators were added as shown in Figure 4.3. Details about the design of these actuators will be discussed in Chapter 5. Both actuators consist of a magnet yoke and a coil unit which move with respect to each other. For arm 1, the magnet yoke is fixed to the world and the coil unit is fixed to this arm. For the actuator driving arm 2, the magnet yoke is fixed to arm 1 and the coil unit is mounted to arm 2. These configurations were chosen because they provide the lowest moving mass and inertia. Coil 2 has been positioned at a distance from the center line of arm 2 such that magnet yoke could be mounted in a stiff manner to arm 1. The vertical positions of the actuators were chosen such that the actuation forces act in line with the CoM of the parts they drive. This aspect avoids unwanted moments about the longitudinal directions of the arms that can result in position errors of the end effector. However, as can be seen in Figure 4.3, the actuators do not vertically align, meaning that the actuation force driving arm 2 causes a moment on arm 1 and vise versa. To minimize these moments, these CoMs of both arms have been aligned as much as possible by making the CoM of arm 1 high and the CoM of arm 2 low to. This has been done by positioning arm 2 closely above the workspace and positioning arm 1 at the top side of the maximum system dimensions. In addition, the bottom side of arm 1 and the top side of arm 2 have been made slanted, which also was done to reduce weight.

Isometric view

Right view

Coil unit 2

Center line arm 2

Magnet yoke 2

Magnet yoke 1

Coil unit 1
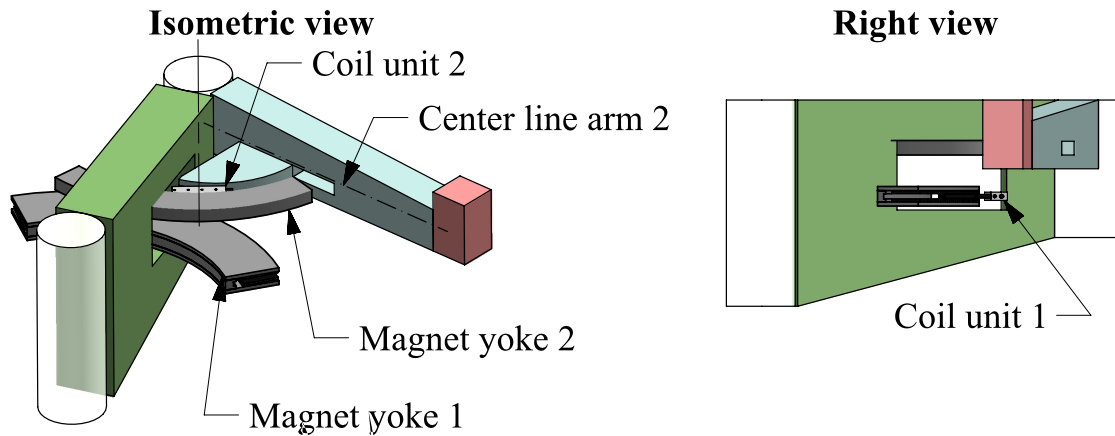
Figure 4.3: New design iteration with added actuators and slanted arms

Figure 4.4 shows the final design iteration of the arms. Both arms have been made narrow near the connection with joint 2 such that they cannot intersect with each other. The part of arm 1 on which magnet yoke 2 is mounted has been made wider to increase bending and torsional stiffness. This wider part has been positioned near magnet yoke 2 to resist against bending forces cause by this actuator, and to provide a stiff mounting surface for this magnet yoke. Furthermore, in Figure 4.4 the arms have been made translucent to show the ribs that have been placed inside both arms to improve stiffness. In general, these ribs were placed such that they avoid out of plane loading of the walls of the arms. In addition, these ribs create multiple 'closed boxes' to increase torsional stiffness. Details about both arms are discussed in the next sections.
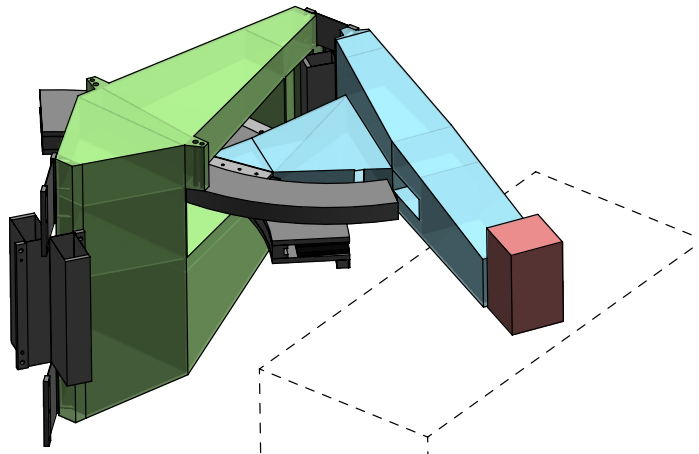
Figure 4.4: Final design iteration with added internal ribs for stiffness

25

4.2 Arm 1
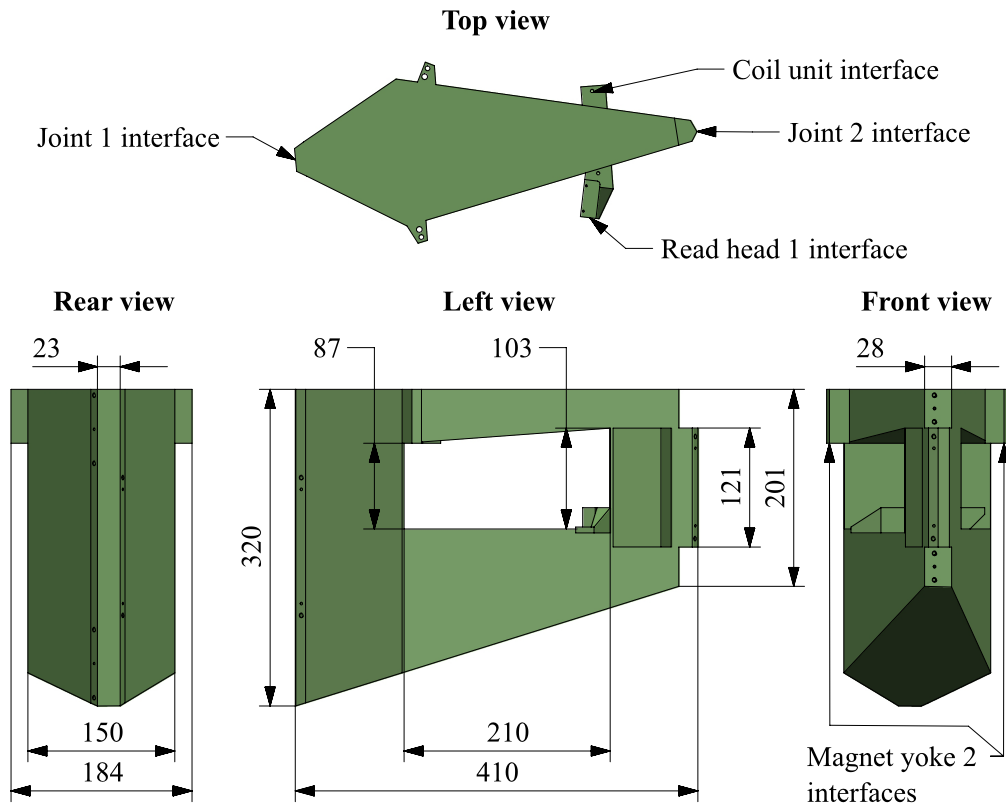
Figure 4.5: Arm 1 design

Figure 4.5 shows the design of arm 1. The front and rear side of this arm connect to joint 1 and 2 respectively, and therefore share the same heights as these joints. The interfaces with the joints are milled aluminum blocks, as shown in the section views of Figure 4.7. To avoid the infinity flexure of joint 2 from intersecting with arm 1, a notch has been made on the side of this arm, as shown in Figure 4.6a. Furthermore, a hole has been made in arm 1 (see Figure 4.5 left view) to fit actuator and sensor components and through which part of arm 2 passes. In this hole, the aluminum block shown in Figure 4.6a holds coil unit 1 and read head 1. Moreover, two blocks at the sides of the arm are used to mount magnet track 2, as shown in Figure 4.6b.

(a)

(b)
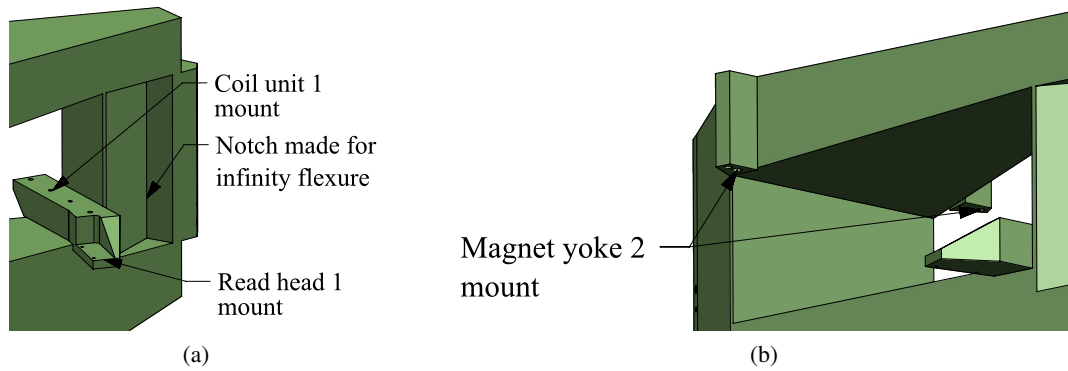
Figure 4.6: Arm 1 interfaces: (a) infinity flexure notch and coil unit 1 and read head 1 mount, (b) magnet yoke 2 mount

For stiffness, multiple ribs have been placed inside of arm 1 to obtain multiple closed boxed, as shown in Figure 4.7. These ribs were placed such that they prevent prevent out of plane loading of the walls of the arm. In addition, the ribs create multiple closed boxes to obtain high torsional stiffness.
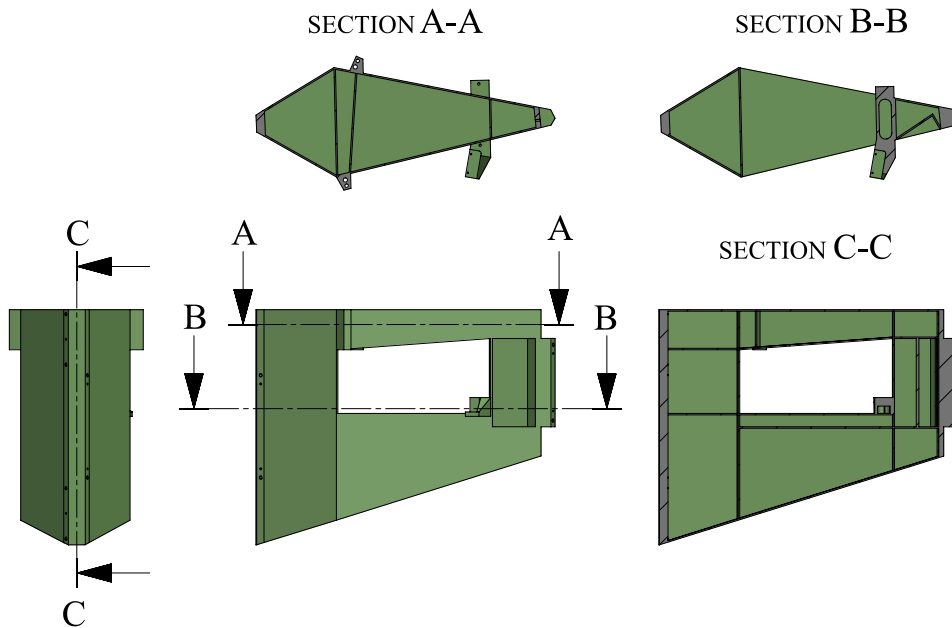
Figure 4.7: Section views arm 1

4.3 Arm 2

Top view (sliced)

Top view

Joint 2
interface

Main structure

(actuator and sensor)
support structure

Coil unit interface

Rear view

Left view

Front view

242

172

200

421

70

60

102

A 48

Encoder scale interface

End effector interface
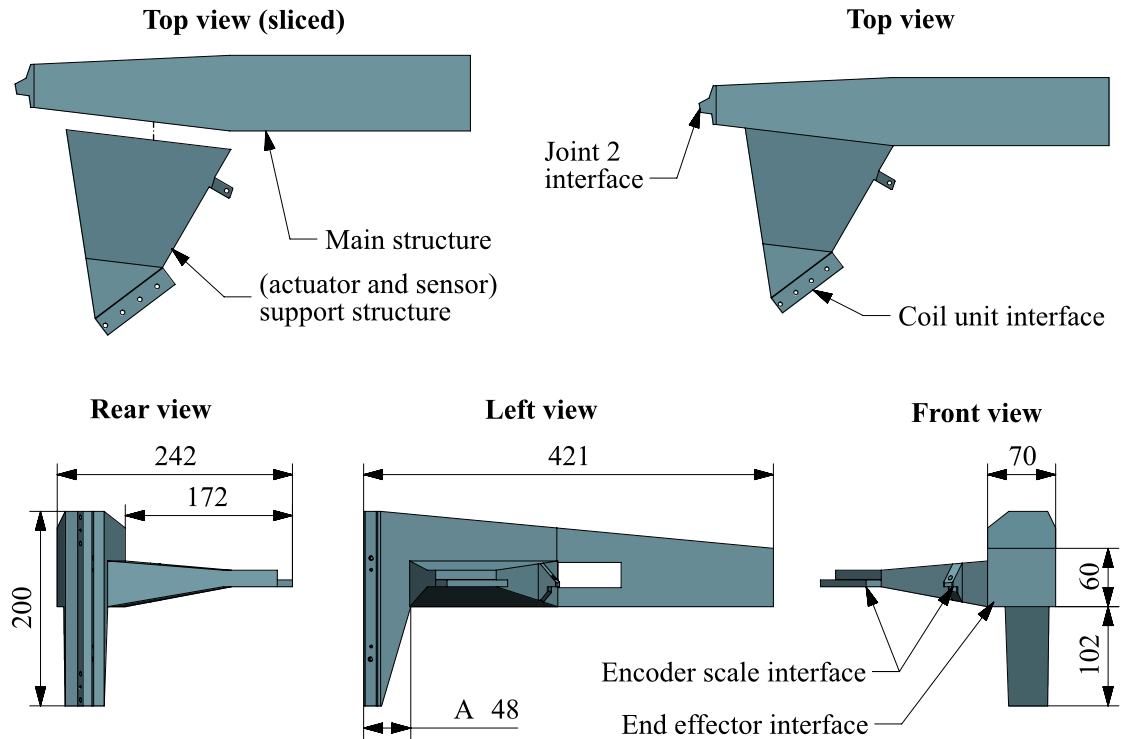
Figure 4.8: Arm 2 design

Figure 4.8 shows the design of arm 2. As can be seen in this figure, arm 2 is distinguished by two parts: first, the main structure that connects to joint 2 and the end effector. Second, the structure that supports the coil unit and the encoder scale, hereafter referred to as the 'support structure'.

The main structure is such that the rear side connects to joint 2 and therefore shares the same height as this joint. Unfortunately, this rear side does not fit above the workspace. Since components of the RR mechanism may not intersect with printed parts, the height of the rear side limits the size of the workspace area. Therefore the length of the rear side, denoted by 'A' in the left view of Figure 4.8, has been made relatively small. Furthermore, a rectangular hole was made in arm 2 (see left view Figure 4.8) for magnet yoke 2 to pass through. Figure 4.9, section view A, shows the ribs that have been fitted inside of the main structure. These ribs were placed to increase stiffness by avoiding out of plane loading of the metal sheets and to avoid deflections of cross sections. Section view A also shows the increased wall thickness made for the interfaces with joint 2 and the end effector.

SECTION A-A

SECTION B-B

SECTION C-C

Figure 4.9: Arm 2 internal structure

The support structure consist of an aluminum block on which the coil unit and the encoder scale are mounted, and a sheet metal part that connects this block to the main structure of arm 2. The support structure has been made such that th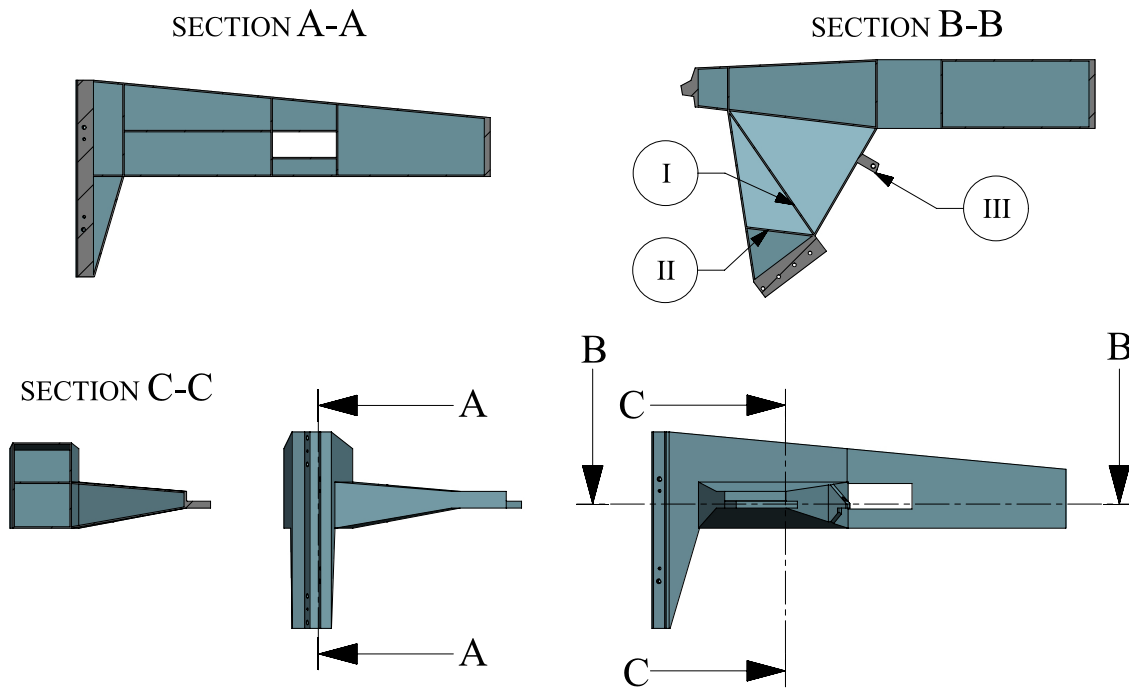e coil unit is mounted at the desired position as explained in Chapter 5. The walls of the support structure connect to the walls and internal ribs of the main structure, as shown in section view B and C of Figure 4.9. Section view B also shows the internal ribs that have been added to the support structure to improve stiffness, which are denoted by the balloons I and II. Finally, an additional aluminum block has been added that is used for mounting of the encoder scale, as denoted by balloon III.

4.4 Conclusions and future work

A conceptual design has been presented for both arms of the RR mechanism. The arms are made from EN AW-6082 T6 aluminum sheet metal. To obtain stiff structures, large cross sectional dimensions have been used and ribs are placed inside of the arms to obtain closed box structures.

If further evaluation of this design is desired, several improvements can be made. First, stress and modal analyses can be used to discover parts that are compliant and parts that might be to stiff. For example, it is expected that holes can be made in the ribs place inside of the arms to reduce weight without noticeably losing stiffness. Furthermore, more detail is required to make the arms manufacturable. Attention must be put into the interfaces with the actuators and the joints to ensure these parts are aligned sufficiently accurate with respect to each other.

5. Actuation system

The function of the actuation system is to drive the rotational DoFs of both arm of the RR mechanism to generate an output motion of the end effector. In this chapter, a conceptual design is proposed for this actuation system. First, various actuator requirements are discussed. Thereafter, an actuation concept is selected and a design is presented. Finally, some concluding remarks are given.

5.1 Requirements

The actuator requirements for the RR mechanism followed from the system requirements specified in Chapter 2.1 and from the joints designed in Chapter 3. Three requirements are considered: minimum rotational velocity, minimum torque, and alignment errors.

5.1.1 Rotational velocity

The system requirements specify that the minimum required translational velocity of the printhead is 0.5 m/s during travel motion. From this requirement, the maximum possible rotational velocities of the joints of the RR mechanism have been deduced, as described in Appendix F. As the actuators move with the same rotational velocities as the joints, these values correspond with the minimum required actuator velocities. For actuator 1 and 2, the minimum required rotational velocities are 1.82 rad/s and 1.76 rad/s respectively.

5.1.2 Torque

Two kinds of torque requirements have been specified for each actuator – peak torque, which the actuator must be able to deliver for a short period, and continuous torque. The continuous requirements have been defined as the maximum possible torques during printing motion. During printing, the maximum linear velocity is 0.25 m/s and the maximum linear acceleration is 5 m/s^2. The maximum possible torques during printing represent the worst-case end effector trajectory. The peak requirements are given by the maximum possible torques during travel (non-printing) motion Here, the maximum linear velocity is 0.5 m/s and the maximum linear acceleration is 10 m/s^2. Travel motions have a short duration and can therefore use torques that exceed the maximum continuous specifications without overheating the motors.

The values of the torque requirements are deduced in Appendix F, and are listed in Table 5.1. In addition, Figure 5.1 plots the maximum required torques for both actuators, depending on the position of the end effector. As can be seen in this figure, the worst-case torque values occur locally, indicating that efficient trajectory planning can significantly reduce the continuously required torques. Further research on efficient trajectory planning is therefore recommended.

Table 5.1: Minimum required actuator torques

	Continuous	Peak
Torque requirement actuator 1 [Nm]	16.75	26.67
Torque requirement actuator 2 [Nm]	8.37	11.89
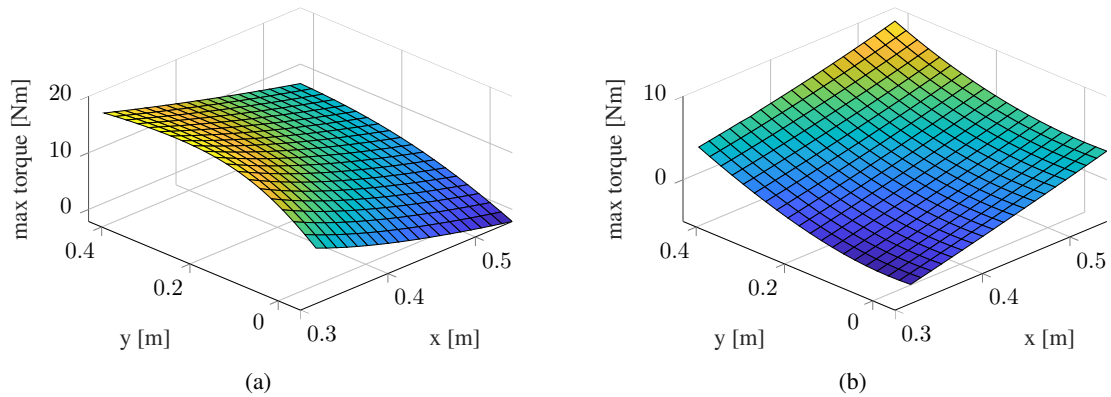
Figure 5.1: Maximum continuous torques plotted across the workspace: (a) actuator 1, (b) actuator 2.

5.1.3 Alignment

All actuators must be able to cope with the radial parasitic motions of the compliant joints. A prediction of these parasitic motions has been made using SPACAR, as depicted in Figure 5.2. Furthermore, the position dependent stiffnesses of the compliant joints and the changing dynamics of the RR mechanism could cause misalignment of actuator components. The actuators must be able to handle these alignment errors.
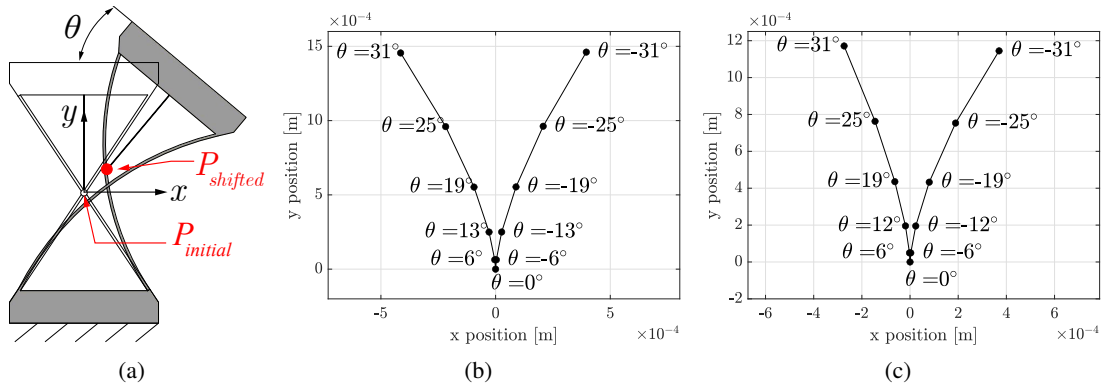
Figure 5.2: Shift of the point P, which for deflection angle $\theta = 0$ represents the initial center of rotation: (a) Schematic representation of the shift of point P with respect to the coordinate frame of the initial center of rotation, (b) shift point P joint 1, (c) shift point P joint 2.

5.2 Actuation concept

To maintain the benefits of the compliant joints, the actuators should not add any sources of friction, play, or vibrations. Common electric rotary motors that operate at a high rotational velocity are therefore not suitable, since they rely on components such as bearings and transmissions. Conversely, Lorentz force type actuators such as voice coils and linear motors are highly suitable since they do not require any tribological contacts.

Lorentz motors are distinguished by iron core and ironless types, of which the iron core motors are typically more economic for a given motor constant. However, the lower price comes at the expense of parasitic forces parallel to the drive direction (cogging) and in the direction of the air gap between the coil and the magnets (pull-in). These forces can significantly increase the joint loads and can affect the position accuracy of the end effector. Hence, ironless motors are preferred. To generate a stroke of 60°, a multi phase motor is desired to achieve an approximately uniform motor constant. Two multi-phase Lorentz actuator concepts are shown in Figure 5.3. The first concept is a so-called torque motor which has a radial air gap between the coils and the magnets. The second concept is a linear motor with an arc-shaped magnet track. The disadvantage of the torque motor is that it is not suitable for the large radial misalignments caused by the joints as this could result in collision between the coils and the magnets. The linear motor concept does not suffer from this problem and has therefore been selected.
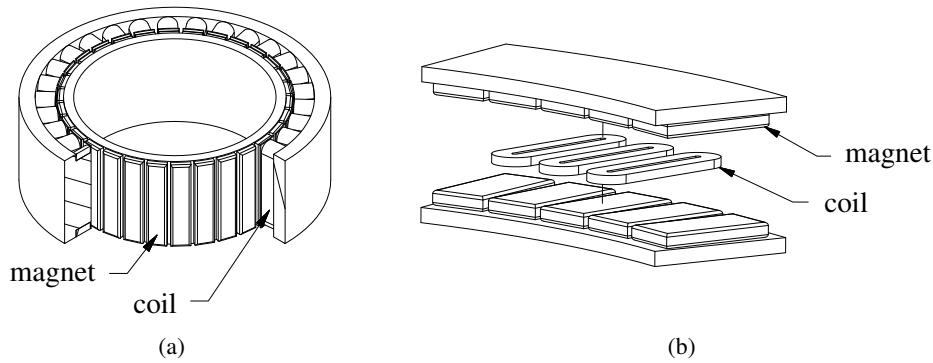
Figure 5.3: Lorentz force-based actuator concepts; (a) torque motor with radial air gap (section view), (b) Linear motor with axial air gap (exploded view).

5.3 Design

No commercially available actuator was found that that meets the concept described in Section 5.2 and is sufficiently small to fit the RR mechanism. To obtain a feasible concept, coil units of linear motors (without a curved magnet track) have been selected for which a custom magnet yoke has to be designed. The selected motors are the Tecnotion UL3 and UM3 for arm 1 and 2 respectively, some of their key properties are listed in Table 5.2. The dimensions of the original magnet yokes corresponding to these actuators are scaled to estimate the dimensions and the mass of the actuation system. The following subsections will describe the implementation of these actuators in the RR mechanism.

Parameter	Continuous force [N]	Peak force [N]	Maximum speed [$\mathrm{m\,s^{-1}}$]	Reference
UL3	240	70	5	[27]
UM3	100	29	10	[28]

Table 5.2: Tecnotion linear motors

5.3.1 Actuator 1

Figure 5.4 shows the design of actuator 1, consisting of coil unit 1 and magnet yoke 1. As explained in Chapter 4, the coil unit is fixed to arm 1 and the magnet yoke is fixed to the world. The center of the arc of the magnet yoke is positioned in line with the initial center of rotation of joint 1. To obtain the required actuation torque of 16.75 N m using a force of 100 N, the actuation force must act at a minimum radius R_1 of

$$R_1 = 16.75/100 = 0.1675 \mathrm{m}.$$

However, a larger radius decreases actuation forces and shortens the force path from the actuator to the end effector, which reduces deflections of arm 1. The actuator radius was therefore chosen so large that it could still be implemented in arm 1 and its components did not interfere with the
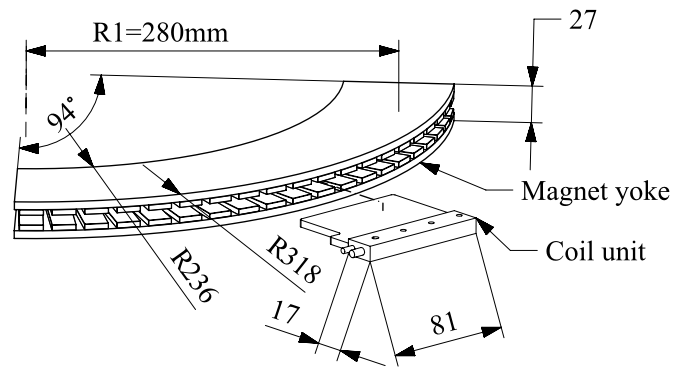
Figure 5.4: Actuator 1 design (exploded view)

workspace or the maximum system dimensions. To further shorten the force path from the actuator to the end effector, the 'open' side of the magnet yoke is positioned at its outer radius. Thereby, the coil unit can be mounted closer to the end effector. The resulting actuation radius is 280 mm. Note that the required continuous torque can also be achieved with this radius. The maximum linear velocity at the actuator radius is $1.82 \cdot 0.28 = 0.51$ m/s, which shows that the velocity requirements are also met.

As explained in Chapter 4, the vertical position of actuator 1 is preferably aligned with the CoM of the RR mechanism. However, exact alignment could not be achieved as the magnet yoke would interfere with arm 2. Therefore the vertical position was chosen such that it as close as possible without interfering with other components, As shown in Figure 5.5, the height difference between the actuation force and the CoM of the RR mechanism is 19.8mm.
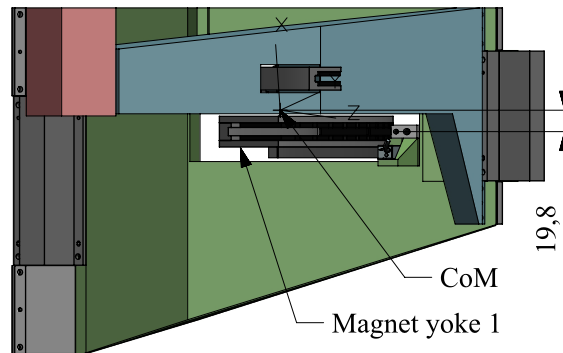
Figure 5.5: Vertical alignment actuator 1

5.3.2 Actuator 2

Figure 5.6 shows the design of actuator 2 that consists of coil unit 2 and magnet yoke 2. As explained in Chapter 4, the coil unit is mounted to arm 2 and the magnet yoke to arm 1. The center

34
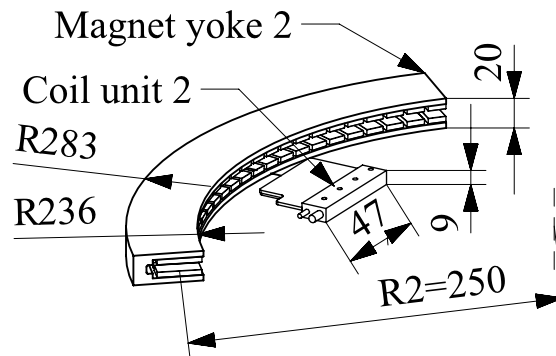
Figure 5.6: Actuator 2 design (exploded view)

of the arc of magnet yoke 2 aligns with the initial center of rotation of joint 2. To obtain the required continuous torque of 8.37 N m using a force of 29 N, the minimum actuation radius R_2 must be

$$R_2 = 8.37/29 = 0.289m.$$

However, this radius adds a significant amount of weight to the RR mechanism and it was impractical to implement due to the size of the magnet yoke. Using a stronger actuator did not show significant improvements of these aspects, as they typically have larger coil units (larger magnet tracks) or require larger magnets (add weight). As an alternative, the radius of the actuator was decreased to 250 mm, with which a maximum torque of 7.25 N m can be achieved. As was shown in Figure 5.1, 8.37 N m is only required for a small part of the workspace area of the RR mechanism. With the selected radius, sufficient torque can be provided for 99% of the workspace area, the added weight is limited, and the actuator can be implemented in a practical manner. Note that the peak torque requirement can be achieved of the entire motion range using this radius. Finally, the maximum linear velocity at the actuator radius is $1.76 \cdot 0.25 = 0.44$ m/s, which shows that the velocity requirements are met. Finally, actuator 2 has been vertically aligned with the CoM of the arm 2 assembly, as shown Figure 5.7.
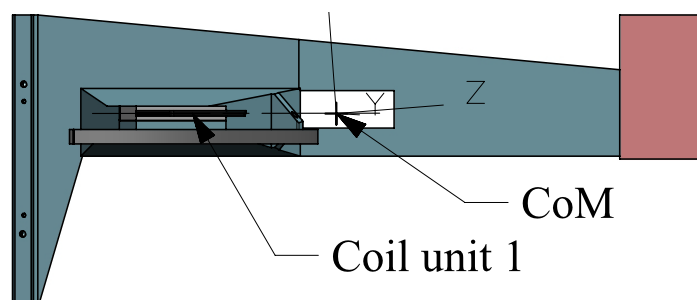
Figure 5.7: Arm 2 assembly: alignment coil unit with CoM

5.4 Conclusions and recommendations

5.4.1 Conclusion

A conceptual design of the actuator system has been obtained for the RR mechanism. A key aspect in the selection type of actuator was that the actuators should not add any sources of friction, backlash, or vibrations to maintain the benefits of the compliant joints. In addition, the actuators must be able to deal with the radial parasitic motions of the joints. Linear Lorentz force motors were selected because they do not add sources of friction or backlash and because these actuators can handle radial misalignments. Iron less type Lorentz motors were selected as they do not exhibit cogging or pull-in forces, which is desired for position accuracy and for the loads placed on the joints.

5.4.2 Recommendations and future work

Section 5.3.2 showed that the required actuation torques cannot be achieved for 1% of the work space area. If this is undesired, it is highly recommended to reduce the weight of arm 2. An alternative is to decrease the maximum torque constraint of the joint 2, such that the optimization algorithm can find a joint design with which the actuators do deliver sufficient torque. However, this will result in a less stiff joint, which is disadvantageous for position accuracy.

To obtain a feasible concept of the RR mechanism, the magnet yokes shown in this chapter are models that are scaled according to dimensions of the non-curved magnet tracks corresponding to the selected coil units. If further evaluation of the RR mechanism is desired, the magnet yokes have to be designed. Special attention must be given to the deflections of the joints such that the coil unit and the magnet will not intersect. In addition, if the coil unit runs out of the magnetic field, the actuator will lose strength. The magnet yokes (and possibly also the coil units) should be designed such the radial parasitic motions will not result in the coil running out of the magnetic field.

6. Measurement system

The measurement system is used to determine the position of the print head relative to the print bed. In this chapter, a measurement system concept is proposed for the RR mechanism. First, the requirements of this system are discussed. Next, a measurement concept is selected, different sensors are compared, and a design is presented. Finally, some concluding remarks are given.

6.1 Requirements

The velocity and alignment requirements of the measurement system are equal to those of the drive system, see Chapter 5.1. Apart from these requirements, a save error budget was assumed for the measurement system of 10% of the total maximum end effector position error. Hence, the measurement system may cause a position error of 5 μm

6.2 Concept

Multiple considerations have been made for the measurement system. First, similar to the drive system, the measurement system should not add sources of friction or vibrations to maintain the benefits of the compliant joints. Hence, a contactless measurement system is preferred. Furthermore, commercially available parts are preferred over custom parts. Finally, a measurement system is preferred that meets the Abbe Bryan principle [29] that, in short, states that a position measurement should be performed in line with the point that has to be measured. However, the RR mechanism is unfortunately not ideal for performing in Abbe measurements due to its serial kinematic design. Although solutions exist that can perform these measurements such as two DoF encoder grids or camera vision, they are often too complex and overqualified for this application. To allow for using less complex sensors, the joint deflection angles are measured to determine the position of the end effector.

Rotary sensors typically require accurate alignment between their moving and the stationary parts. To be able to deal with the parasitic motions of the joints, several linear encoder concepts have been considered, an example of which is shown in Figure 6.1. These encoders use a reading head that measures its relative position or displacement to a scale. For different off the shelf linear encoders, this scale can be mounted to a curved surface. If this curved surface follows the parasitic motion of the joint, it is expected that sufficient alignment can be maintained between the read head and the scale.

Figure 6.1: Linear encoder concept, source RLS: [30]

6.3 Design
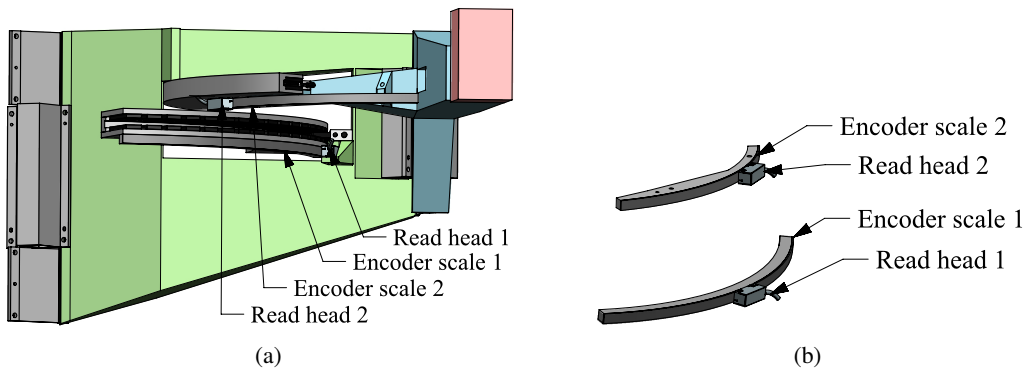
Figure 6.2: Linear encoders mounted to RR mechanism

Before comparing different sensors, the design of the measurement system is first shown to clarify different considerations for the sensor selection. Figure 6.2 shows the linear encoders, which are mounted to the actuators of the RR mechanism. Apart from being practical, these positions have been chosen because the actuators provide an interface with a large radius. With linear encoders used for measuring rotations, a larger radius of the scale results in a larger angular resolution. The sensors are mounted such that the read heads are positioned at the outer sides of the radii of the scales, as shown in Figure 6.3b. This has been done to minimize the height difference between the reading part and the scale, which is desired for accuracy and stability of the encoder.
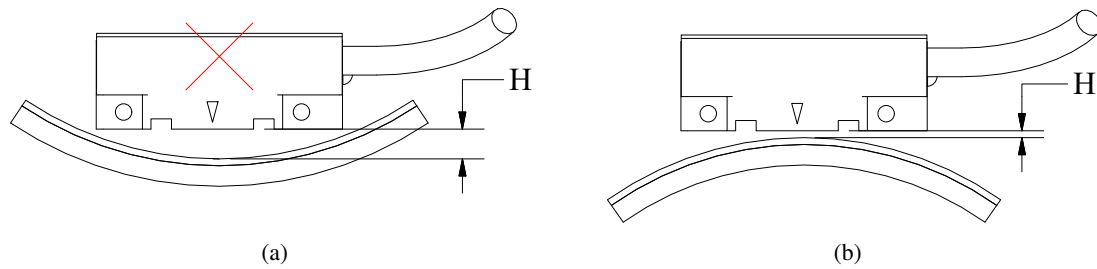
Figure 6.3: Encoder scale mounting, H denotes the height difference between the scale and the reading part of the sensor: (a) undesired configuration, (b) desired configuration.

Both encoder scales are mounted to an aluminum part that will be milled to follow the radial parasitic motion of the joints. The minimum radii of encoder scale 1 and 2 is 317 mm and 235 mm respectively, which followed from the actuators on which they are mounted. Typically encoder scales are available with adhesive such that they can be fixed to this aluminum part.

6.3.1 Sensor selection

For the selection of sensors, first the sensor accuracy requirements have been estimated using the error budget described in Section 6.1. This estimation is described in Appendix F, the resulting requirement for sensor 1 and 2 are 3.78 µm and 2.47 µm respectively. This requirement holds after calibration of the measurement system. Therefore, different sensors have been evaluated based on their resolution. An estimation was made that the sensors must have a resolution that is at least ten times smaller than the required accuracy, hence the minimum required resolutions for sensor 1 and 2 are 0.378 µm and 0.247 µm respectively.

Different commercially available linear encoders have been considered, of which three are listed in Table 6.1. As can be seen in this table, these sensors meet the estimated resolution requirements as described above. Apart from their resolution, the sensors have been compared based on their alignment tolerances, see Figure 6.4 for these tolerances. Due to the position varying stiffnesses of the joints and the varying dynamics of the RR mechanism, the encoder scales and read heads can move with respect to each other (apart from the radial parasitic motion of the joints). For robustness of the measurement system, a sensor is desired that can handle misalignments. As can be seen in Table 6.1, the RLS LM13 magnetic incremental encoder can handle the largest misalignments. Although this sensor does not have the highest resolution of the considered sensors, it is expected to provide sufficient accuracy. Therefore, this sensor has been selected.
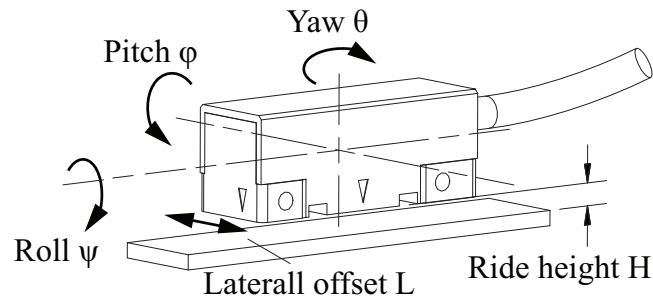
Figure 6.4: Encoder alignment tolerances

Table 6.1: Linear sensors

Manufacturer	Heidenhain	Renishaw	RLS
Product code	LIC2119	RKLC40-S	LM13
Transducer	Optical	Optical	Magnetic
Type	Absolute	Incremental	Incremental
Accuracy (without calibration) [μm]	15	15	10
Resolution [μm]	0.05	0.05	0.224
Max ride height offset (H) [±mm]	0.5	0.2	0.7
Max lateral offset (L) [±mm]	1	0.5	1
Max roll offset (ψ) [±°]	1	0.8	3
Max pitch offset (ϕ) [±°]	1	1	3
Max Yaw offset (θ) [±°]	1	0.9	1

6.4   Conclusions and recommendations

A conceptual measurement system was obtained in this chapter. A key aspect of the selection of the sensors was that the measurement system should not add any friction to the system to maintain the benefits of the compliant joints. Furthermore, the sensors must be able to deal with the radial parasitic motions and other undesired deflections of the joints. Therefore, linear encoders have been selected from which their encoder scale is mounted to a curved surface which follows the radial motion of the joints. In addition, this sensor type was selected because it is expected to provide sufficient accuracy and because it can handle relatively large misalignments.

If this design will be further evaluated, it is essential to validate if the deflections of the joints will not impair the functionality of the sensors. In addition, even though the accuracy requirements are based on save assumptions, validation of the accuracy still desired to test if the accuracy requirements of the RR mechanism can be met.

7. Conclusions and future work

The goals of this thesis were to obtain a design method for large stroke compliant joints in accurate motion systems, and to study critical design aspects and potential risks for implementing large stroke compliant joints in these systems. To obtain, test, and demonstrate these aspects, a large stroke two DoF translation stage had to be designed that uses compliant joints for guidance. The results from this thesis can be divided by two parts: a theoretical part consisting of a design method for compliant joints in accurate motion systems, and a practical design of the translation stage to identify the critical design aspects and risks.

The joint design method was described in Chapter 3. First, the properties of the joints were investigated that are crucial for evaluating complaint joints for accurate motion systems. The main takeaway was that special attention must be given to maximum internal stresses, parasitical motions, actuation torque, and most importantly the first unwanted eigenfrequency of the joint. A selection of both common and uncommon joints was evaluated in this thesis. These joints were evaluated using an optimization algorithm. The objective was to maximize the first unwanted eigenfrequency over the stroke of the motion range, while satisfying multiple constraints such as the stress limits or manufacturability properties.

For the design of a translation stage, the so-called 'RR mechanism' concept has been selected, which consists of two arms connected in series and two actuated rotational joints. This mechanism can achieve a great workspace area within the limited space of this project, using only a few number of components. Although the initially required workspace area could not be achieved, a workspace area was established that is only 14% smaller. An optimization algorithm was used in combination with a parametric kinematic model of the RR mechanism to maximize the size of the workspace area.

For both joints of the RR mechanism, the so-called 'Infinity hinge' concept has been selected, as it performed the best in terms of first unwanted eigenfrequency after optimization. The arms of the RR mechanism are aluminum sheet metal structures. The design of the arms include large cross sectional dimensions to obtain high stiffness and low mass. In addition, the structures of the arms include multiple closed boxes to increase torsional stiffness.

Actuators have been selected for the RR mechanism such that the advantages of the compliant joints (e.g. no friction and no backlash) were maintained. In addition, the actuators had to be able to deal with the radial parasitic motions of the compliant joints. Therefore, linear Lorentz force motors have been selected, as they do not require any tribological contacts and they are able to deal with the parasitic motions of the joints.

Finally a measurement system was designed. Similar to the drive system, the measurement system should not add any sources of friction and it should be able to deal with the radial parasitic motions of the joint. Therefore linear encoders have been used from which the encoder scale is mounted to a curved surface which follows this radial motion.

7.1 Future work

The motion accuracy requirements specified in Chapter 2.1.3 have unfortunately not been validated. The attempt made for this validation has not been finished within the time frame of this project. To ensure the system works as specified, this validation is highly recommended.

For the design of the compliant joints, the primary focus was on obtaining optimal geometry parameters. However, material and fatigue properties also significantly determine the performance of a compliant joint. Further research on the material and fatigue properties are therefore recommended, some research suggestions are given in Chapter 3.4.

The joint optimization results from Chapter 3 showed that the performance of different types of joints can significantly vary. Evaluating other types of joints could therefore result higher performing joints. Appendix E shows multiple types of compliant joints that are highly recommended for further evaluation.

The design of the RR mechanism was made on a conceptual level. If further evaluation of this mechanism is desired, more detail must be put into the design. First, all components must be made manufacturable. Furthermore, the magnet yokes of the RR mechanism have to be designed. Next, the arms can be optimized in terms of weight and stiffness. Finally, the stability of measurement system in relation to the deflections and parasitical motions of the joints should be tested.

References

[1] J. A. Haringx. The cross spring pivot as a constructional element. *Applied scientific Research*, A1:313–332, 1948.

[2] L. Howell, S. P. Magleby, and B. M. Olsen. *Handbook of compliant mechanisms*. John Wiley & Sons, Inc, Chichester, West Sussex, United Kingdom Hoboken, New Jersey, 2013.

[3] J. van Eijk. *On the Design of Plate-spring Mechanisms*. Technische Hogeschool Delft, 1985.

[4] H.M.J.R. Soemers. *Design principles : for precision mechanisms*. Herman Soemers, S.l, 2011.

[5] K.G.P. Folkersma, S.E. Boer, D.M. Brouwer, J.L. Herder, and H.M.J.R. Soemers. A 2-dof large stroke flexure based positioning mechanism. In *ASME 2012 International Design Engineering Technical Conferences and Computers and Information in Engineering Conference*, pages 221–228, United States, August 2012. American Society of Mechanical Engineers (ASME). 36th Mechanisms and Robotics Conference, MECH 2012, MECH ; Conference date: 12-08-2012 Through 15-08-2012.

[6] D. H. Wiersma, S. E. Boer, R. G. K. M. Aarts, and D. M. Brouwer. Design and Performance Optimization of Large Stroke Spatial Flexures. *Journal of Computational and Nonlinear Dynamics*, 9(1), 11 2013. 011016.

[7] Jacob Philippus Meijaard, Dannis Michel Brouwer, and Jan B. Jonker. Analytical and experimental investigation of a parallel leaf spring guidance. *Multibody system dynamics*, 23(1):77–97, 2010.

[8] Morgan D. Murphy, Ashok Midha, and Larry L. Howell. The topological synthesis of compliant mechanisms. *Mechanism and Machine Theory*, 31(2):185 – 199, 1996.

[9] P. Spanoudakis, L. Kiener, F. Cosandier, P. Schwab, L. Giriens, J. Kruis, D. Grivon, G. Psoni, C. Vrettos, and N. Bencheikh. Large angle flexure pivot development for future science payloads for space applications. *MATEC Web of Conferences*, 304:07016, 2019.

[10] M. Naves, R.G.K.M. Aarts, and D.M. Brouwer. Large stroke high off-axis stiffness three degree of freedom spherical flexure joint. *Precision Engineering*, 56:422 – 431, 2019.

[11] M. Naves, M. Nijenhuis, W.B.J. Hakvoort, and D.M. Brouwer. Flexure-based 60 degrees stroke actuator suspension for a high torque iron core motor. *Precision Engineering*, 63:105 – 114, 2020.

[12] M. Naves, D. M. Brouwer, and R. G. K. M. Aarts. Building Block-Based Spatial Topology Synthesis Method for Large-Stroke Flexure Hinges. *Journal of Mechanisms and Robotics*, 9(4), 05 2017. 041006.

References

[13] F. Fennis. Private communication, 2020.

[14] M. Spong, S. Hutchinson, and M. Vidyasagar. *Robot modeling and control*. John Wiley & Sons, Hoboken, NJ, 2006.

[15] J. A. Nelder and R. Mead. A Simplex Method for Function Minimization. *The Computer Journal*, 7(4):308–313, 01 1965.

[16] J. B. Jonker and J. P. Meijaard. *SPACAR — Computer Program for Dynamic Analysis of Flexible Spatial Mechanisms and Manipulators*, pages 123–143. Springer Berlin Heidelberg, Berlin, Heidelberg, 1990.

[17] S. T. Smith. *Flexures : elements of elastic mechanisms*. Gordon & Breach, New York, 2000.

[18] Hedzer Wiersema, Ronald Aarts, Steven Boer, and Dannis Brouwer. Flexure joint for high precision relative movement of devices or parts of devices, 6 2014.

[19] Sioux Technologies. Internal documents, 2018.

[20] Todd Mower. Degradation of titanium 6al-4v fatigue strength due to electrical discharge machining. *International Journal of Fatigue*, 64, 07 2014.

[21] Gerd Lütjering and James C. Williams. *Titanium*. Springer Berlin Heidelberg, 2003.

[22] Uddeholm. Stavax esr. Datasheet, 10 2013.

[23] AK Steel. 301 stainless steel. Datasheet, 12 2016.

[24] A Beek. *Advanced engineering design : lifetime performance and reliability*. TU Delft, Delft, 2009.

[25] W.D. Callister and D.G. Rethwisch. *Materials Science and Engineering: An Introduction, 8th Edition*. Wiley, 2009.

[26] M. F. Ashby. *Materials : engineering, science, processing and design*. Butterworth-Heinemann, Kidlington, Oxford, United Kingdom Cambidge, MA, United States, 2019.

[27] Tecnotion. Ul series ironless. Datasheet, 2016.

[28] Tecnotion. Um series ironless. Datasheet, 2016.

[29] J.B. Bryan. The abbé principle revisited: An updated interpretation. *Precision Engineering*, 1(3):129 – 132, 1979.

[30] Lm13 incremental magnetic encoder. https://www.rls.si/eng/lm13-magnetic-linear-and-rotary-encoder-system. Accessed: 2021-01-5.

[31] Peter Spanoudakis, Lionel Kiener, Florent Cosandier, Philippe Schwab, Laurent Giriens, Johan Kruis, Daniel Grivon, Georgia Psoni, Christos Vrettos, and Nabil Bencheikh. Large angle flexure pivot development for future science payloads for space applications. *MATEC Web of Conferences*, 304:07016, 01 2019.

[32] Simon Henein, Peter Spanoudakis, Serge Droz, Leif Myklebust, and Emmanuel Onillon. Flexure pivot for aerospace mechanisms. *European Space Agency, (Special Publication) ESA SP*, 01 2003.

[33] Steven Boer, Ronald Aarts, D.M. Brouwer, and Ben Jonker. Multibody modelling and optimization of a curved hinge flexure. *The 1st Joint International Conference on Multibody System Dynamics, Lappeenranta, Finland, May 25-27, 2010*, pages 1–10, 01 2010.

[34] Mathijs Fix, Dannis Brouwer, and Ronald Aarts. Building block based topology synthesis algorithm to optimize the natural frequency in large stroke flexure mechanisms, 08 2020.

[35] Brian P. Trease, Yong-Mo Moon, and Sridhar Kota. Design of large-displacement compliant joints. *Journal of Mechanical Design*, 127(4):788–798, November 2004.

[36] N. van de Wouw. Multibody dynamics - lecture notes, 2016.

A. Alternative design configurations

In this appendix, multiple alternative design configurations are shown that have been made for the translation stage.
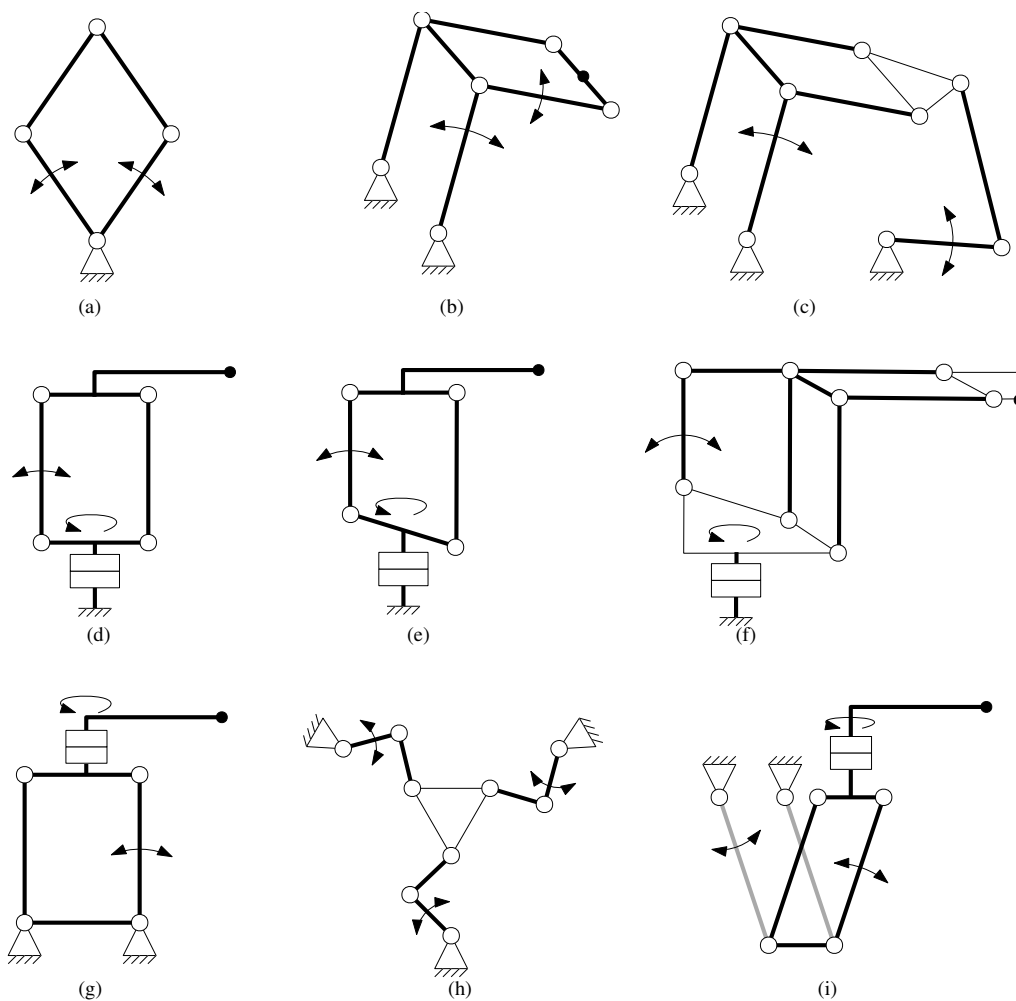
Figure A.1: Translation stage layout concepts

Figure A.1 shows multiple conceptual layouts that have been considered for the flexure based translation stage. Most of these concepts were primarily not selected due to their small operating range, their high part count. In addition, some mechanisms were not selected as they exhibit parasitical motions. To compare the workspace areas of multiple mechanisms, optimization was used similar to the method shown appendix B.

B.   Topology optimization RR mechanism

Finding a set of design parameters for the flexure-based RR mechanism such that its workspace area is as large as possible is difficult to achieve analytically. Therefore, an optimization algorithm has been deployed in MATLAB®to find a set of optimal parameters using a kinematic model. In this appendix, the optimization method, kinematic model, and the resulting optimal parameters are discussed.

B.1   Optimization criteria

Symbol	Parameter
O	joint 1 node
A	joint 2 node
B	end effector node
W	workspace center node
r_1	radius joint 1
r_2	radius joint 2
r_3	radius end effector
r_4	radius constraint joint 2 and arms
f_1	x-dimension footprint
f_2	y-dimension footprint
l_1	length arm 1
l_2	length arm 2
s_x	x-stroke
s_y	y-stroke
θ_1	orientation joint 1
θ_2	orientation joint 2
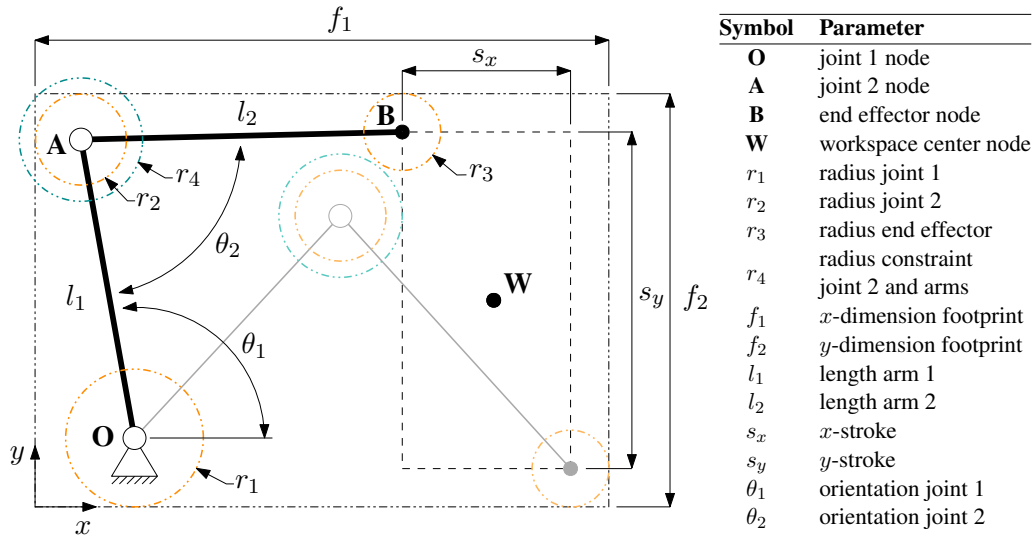
Figure B.1: RR mechanism layout and parameters (top view). The black and gray mechanism drawings show two possible configurations

The goal of the optimization was to find a set of parameters $\boldsymbol{p}$ for which the rectangular workspace area is as large as possible. Figure B.1 shows the RR mechanism and the associated parameters. A set of six variables has been used to describe the geometry of the mechanism:

$$\boldsymbol{p} = \begin{bmatrix} l_1 & l_2 & s_x & s_y & W_x & W_y \end{bmatrix},$$

where W_x and W_y describe the center coordinates of the workspace. An additional parameter can be used to describe the orientation of the workspace; however, this parameter has been omitted as it did not improve results from optimization. This effect suggests that solutions where the borders of the workspace are parallel to those of the footprint are the most space-efficient. The workspace area is therefore oriented as illustrated in Figure B.1.

Most optimization algorithms aim at minimizing a given function. The objective function $\mathcal{F}(\boldsymbol{p})$ is therefore defined as the inverse of the workspace area

$$\mathcal{F}(\boldsymbol{p}) = \frac{1}{s_x s_y}.$$

Furthermore, results returned by the optimization algorithm may not violate the following constraints:

1. The footprint dimension f_1 may not exceed 0.78 m, see Chapter 2.1.
2. The footprint dimension f_2 may not exceed 0.55 m, see Chapter 2.1.
3. The range of θ_1 and θ_2 may not exceed $\theta_{\max}$ to prevent failure of the joints.
4. The blue circle around joint 2 with radius r_4 may not enter the workspace area to avoid components of the RR mechanism from colliding with printed parts. The design of arm 1, joint 2, and part of arm 2 have become to high to be positioned above the workspace; hence, this requirement was necessary.

These attributes define the following set of constraints

$$\mathcal{C}(\boldsymbol{p}) = \left\{ \begin{array}{c} f_1 - 0.55 \\ f_2 - 0.78 \\ |\theta_{1,max}(\boldsymbol{p}) - \theta_{1,min}(\boldsymbol{p})| - \theta_{max} \\ |\theta_{2,max}(\boldsymbol{p}) - \theta_{2,min}(\boldsymbol{p})| - \theta_{max} \\ g(\boldsymbol{p}) \end{array} \right\}, \tag{B.1}$$

where $g(\boldsymbol{p})$ is a measure for how much the blue circle enters the workspace, see Section B.2. A solution is feasible when the entire set of constraints is less than zero for any configuration where the end effector lies inside of the workspace. This defines the following optimization problem

$$\boldsymbol{p}_{\mathrm{opt}} = \arg \min_{\boldsymbol{p}} \mathcal{F}(\boldsymbol{p})$$

$$\text{subject to } \mathcal{C}(\boldsymbol{p}) \leq 0 \; \forall \; \left\{ \begin{array}{l} W_x - s_x/2 \leq x \leq W_x + s_x/2 \\ W_y - s_y/2 \leq y \leq W_y + s_y/2 \end{array} \right\}.$$

B.2 Kinematic model

In this section, a model is derived to determine all parameters required for optimization using the variable set $\boldsymbol{p}$ and the constraint parameters r_1 to r_4. In short, the model works as follows:

1. Numerous end effector positions are uniformly distributed across the workspace.
2. The joint angles and coordinates corresponding to these end effector positions are computed.
3. The minimum and maximum values of θ_1 and θ_2 are determined.
4. The footprint dimensions f_1 and f_2 are derived from the extreme x and y coordinates of the end effector and the joints, taking into account their dimensions r_1 to r_3.
5. The parameter $g(\boldsymbol{p})$ is determined by defining a space which joint 2 may not enter. If joint 2 does enter this 'prohibited' space, the constraint value is given by the maximum distance between joint 2 and the point where arm 1 intersects with the prohibited space
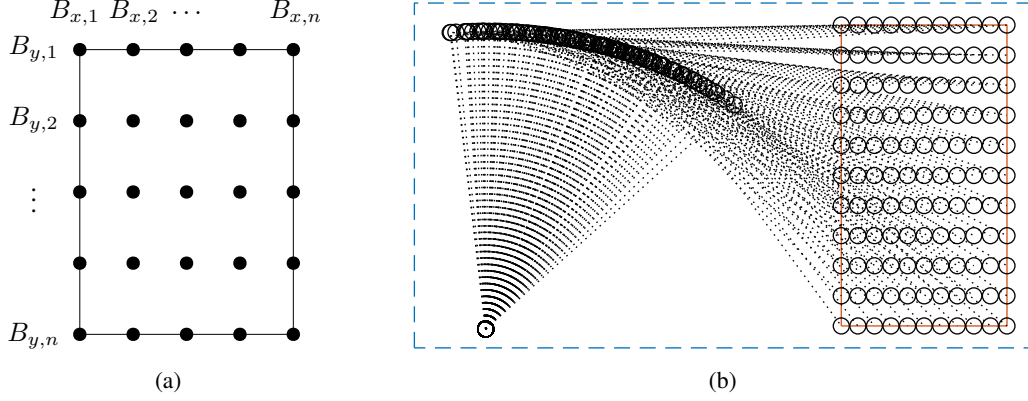
Figure B.2: end effector positions: (a) $n \times n$ end effector position uniformly distributed across the workspace area, (b) end effector positions plotted. The blue, orange and black lines describe the footprint, workspace, and $n \times n$ layout configurations respectively.

The end effector positions are defined by node $\mathbf{B}_{ij} = \begin{bmatrix} B_{x,i} & B_{y,j} \end{bmatrix}^{\mathrm{T}}$ with i & $j \in \{1, 2, \ldots, n\}$. In total n^2 end effector positions are computed in the way illustrated in Figure B.2a. These coordinates are calculated as:

$$B_{x,i} = W_x - \frac{s_x}{2} + s_x \frac{(i-1)}{(n-1)}$$

$$B_{y,j} = W_y - \frac{s_y}{2} + s_y \frac{(j-1)}{(n-1)}.$$

Next, the joint angles $\theta_{1,ij}$ and $\theta_{2,ij}$ corresponding to $B_{x,i}$ and $B_{y,j}$ are calculated using equations (C.3) and (C.4). From these results, the minimum and maximum joint angles are deduced as

$$\theta_{1,\min} = \min_{ij} \theta_{1,ij} \qquad\qquad \theta_{1,\max} = \max_{ij} \theta_{1,ij}$$

$$\theta_{2,\min} = \min_{ij} \theta_{2,ij} \qquad\qquad \theta_{2,\max} = \max_{ij} \theta_{2,ij}.$$

Then, the positions of the joints are computed: the coordinates of joint 1 are described by node $\mathbf{O} = \begin{bmatrix} 0 & 0 \end{bmatrix}^{\mathrm{T}} \; \forall \, ij$ as it is fixed to the origin. Furthermore, the coordinates of joint 2, denoted by node $\mathbf{A}_{ij} = \begin{bmatrix} A_{x,ij} & A_{y,ij} \end{bmatrix}^{\mathrm{T}}$, are computed as

$$\mathbf{A}_{ij} = \begin{bmatrix} l_1 \cos(\theta_{1,ij}) & l_1 \sin(\theta_{1,ij}) \end{bmatrix}^{\mathrm{T}}.$$

Thereafter, the footprint dimensions are computed

$$f_1 = |\max_{ij} \{O_x + r_1, \quad A_{x,ij} + r_2 \quad B_{x,i} + r_3\} -$$
$$\min_{ij} \{O_x - r_1, \quad A_{x,ij} - r_2 \quad B_{x,i} - r_3\}|$$
$$f_2 = |\max_{ij} \{O_y + r_1, \quad A_{y,ij} + r_2 \quad B_{y,i} + r_3\} -$$
$$\min_{ij} \{O_y - r_1, \quad A_{y,ij} - r_2 \quad B_{y,i} - r_3\}|.$$

Finally, the constraint parameter g is computed. The goal of this parameter is to detect if joint 2 comes to close too the workspace and to provide a measure for, if the constraint is violated, how much this constraint is violated. The latter is necessary for convergence of the optimization problem. For this constraint, first, an area is defined which joint 2 (node **A**) may not enter, see Figure B.3. The border of this prohibited space has an offset of r_4 with respect to the workspace.
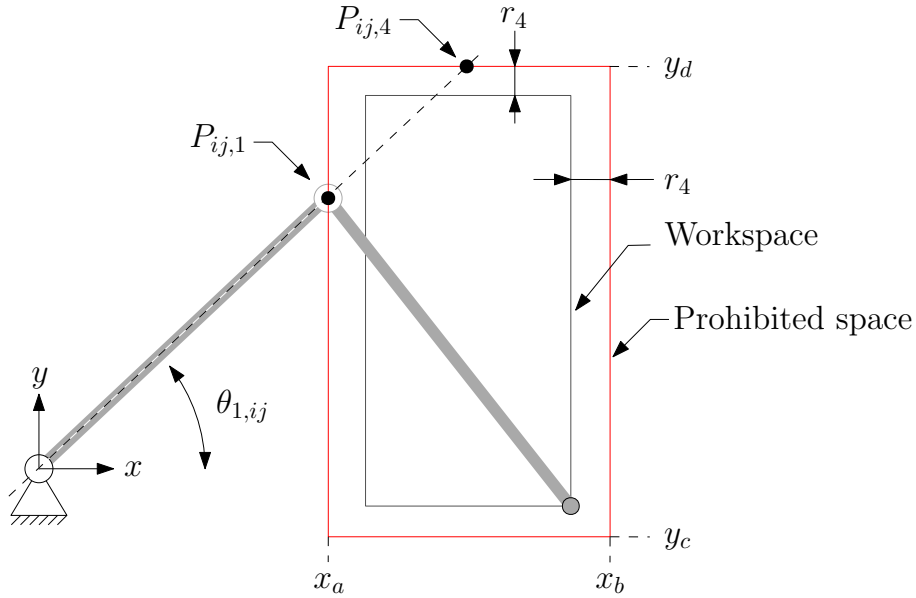
Figure B.3: RR mechanism top view with joint 1 prohibited space (red rectangle)

Then, the intersection points of the line collinear to arm 1 with the borders of the prohibited space are calculated for every $\theta_{1,ij}$, as illustrated in Figure B.3. These points are found by solving

$$P_{ij,1} = \begin{bmatrix} x_a & x_a \tan(\theta_{1,ij}) \end{bmatrix}$$
$$P_{ij,2} = \begin{bmatrix} x_b & x_b \tan(\theta_{1,ij}) \end{bmatrix}$$
$$P_{ij,3} = \begin{bmatrix} \frac{y_c}{\tan(\theta_{1,ij})} & y_c) \end{bmatrix}$$
$$P_{ij,4} = \begin{bmatrix} \frac{y_d}{\tan(\theta_{1,ij})} & y_d), \end{bmatrix}$$

and then by eliminating the points that do not lie on the prohibited space. The x and y coordinates P_x and P_y respectively of every valid point meets the conditions

$$x_a \leq P_x \leq x_b$$
$$y_c \leq P_y \leq y_d.$$

For every valid intersection point the norm is computed $||\mathbf{P}_{ijk}||$, which is the distance from this point to the origin. If this distance is smaller than the length of arm 1, joint 2 lies inside the prohibited space. The parameter g is therefore computed as

$$g(\boldsymbol{p}) = \max_{ijk} \left(l_1 - ||P_{ijk}|| \right),$$

that is the maximum distance between joint 2 and an intersection point of arm 1 with the prohibited space.

B.3   Optimization algorithm

The kinematic model contains nonlinearities and the derivatives of the constraints are unknown. Therefore, optimization algorithms that can solve constrained, nonlinear, derivative free problems can be used. The selected method is the MATLAB®fmincon interior-point algorithm. Other algorithms, such as the Nelder-Mead simplex method [15] and Matlab's patternsearch function have also been tested which gave comparable results. Unfortunately, this optimization problem is not convergent to a global optimum, meaning that its results vary with different initial parameters. To minimize the risk of finding a non-global optimum, the optimization has been performed numerous times using randomly generated initial parameters $\boldsymbol{p}_{in}$.

B.4   Results

The resulting optimal variable parameters and the corresponding constraint parameters are given in Table B.1. All constraints were active, meaning that every constraint limited the size of the workspace.

Table B.1: Optimal variables and constraint parameters

Optimal variables			Constraint/fixed parameters		
l_1	420	mm	r_1	30	mm
l_2	476	mm	r_2	45	mm
W_x	431	mm	r_3	35	mm
W_y	180	mm	r_4	50	mm
s_x	224	mm	$f_{1,\max}$	780	mm
s_y	480	mm	$f_{2,\max}$	550	mm
			n	21	-
			$\theta_{\max}$	60	degree

The fixed parameters have been obtained as follows: the joint radii r_1 and r_2, effector radius r_3, and position constraint r_4 were obtained from the CAD model of the mechanism. Getting these values required iterations between the optimization algorithm and the design of the joints and arms. Furthermore, the parameter n was determined by iteratively increasing this value until no more variations in the output of the kinematic model were observed. Finally, the maximum joint deflection angle is based on the assumption that this angle is feasible for an elastic hinge such that sufficient stiffness is maintained.

B.4.1 Total feasible workspace area
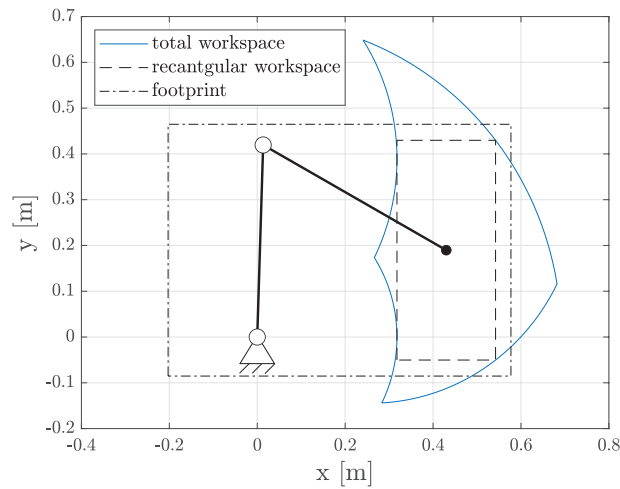
Figure B.4: Total workspace area optimal RR mechanism (top view) when neglecting the maximum footprint dimensions.

The total workspace area of the RR mechanism is larger than the rectangular workspace area considered earlier this section, see Figure B.4. This indicates that the workspace area can be enlarged with only minor modifications to the system, considering the kinematics. If the maximum footprint dimensions are neglected, the surface of the total workspace area is 84% larger than the rectangular workspace area.

C. Kinematic equations RR mechanism

Multiple calculations in this thesis depend on the kinematic equations of the RR mechanism. In this appendix, these kinematic equations are derived.

Figure C.1: RR mechanism layout and parameters. The black and gray mechanism drawings show two possible configurations
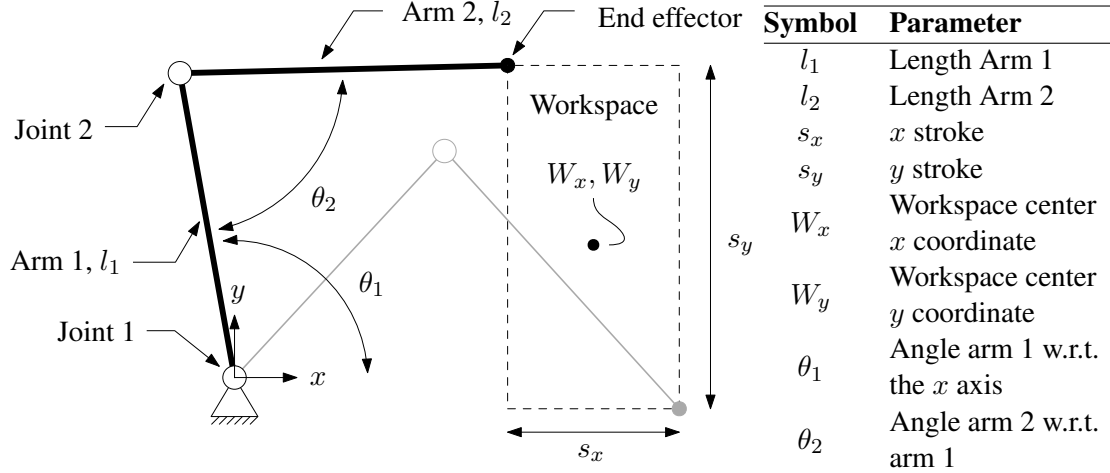
C.1 Forward kinematics

The relation between the joint angles θ_1 and θ_2 and the end effector coordinates x and y are given by (C.1) and (C.2).

$$\begin{aligned}
x &= l_1 \cos(\theta_1) + l_2 \cos(\theta_1 + \theta_2 - \pi) \\
&= l_1 \cos(\theta_1) - l_2 \cos(\theta_1 + \theta_2)
\end{aligned} \tag{C.1}$$

$$\begin{aligned}
y &= l_1 \sin(\theta_1) + l_2 \sin(\theta_1 + \theta_2 - \pi) \\
&= l_1 \sin(\theta_1) - l_2 \sin(\theta_1 + \theta_2)
\end{aligned} \tag{C.2}$$

The end effector velocity v has been determined using the time derivatives of (C.1) and (C.2)

$$\begin{aligned}
v &= \sqrt{\dot{x}^2 + \dot{y}^2} \\
\dot{x} &= -l_1 \sin(\theta_1)\dot{\theta}_1 + l_2 \sin(\theta_1 + \theta_2)(\dot{\theta}_1 + \dot{\theta}_2) \\
\dot{y} &= l_1 \cos(\theta_1)\dot{\theta}_1 - l_2 \cos(\theta_1 + \theta_2)(\dot{\theta}_1 + \dot{\theta}_2).
\end{aligned}$$

Similarly, the accelerations have been computed by taking the time derivatives of the velocity equations

$$a = \sqrt{\ddot{x}^2 + \ddot{y}^2}$$

$$\ddot{x} = -l_1 \sin(\theta_1)\ddot{\theta}_1 - l_1 \cos(\theta_1)\dot{\theta}_1^2 + l_2 \sin(\theta_1 + \theta_2)(\ddot{\theta}_1 + \ddot{\theta}_2)$$
$$+ l_2 \cos(\theta_1 + \theta_2)(\dot{\theta}_1 + \dot{\theta}_2)^2$$

$$\ddot{y} = l_1 \cos(\theta_1)\ddot{\theta}_1 - l_1 \sin(\theta_1)\dot{\theta}_1^2 - l_2 \cos(\theta_1 + \theta_2)(\ddot{\theta}_1 + \ddot{\theta}_2)$$
$$+ l_2 \sin(\theta_1 + \theta_2)(\dot{\theta}_1 + \dot{\theta}_2)^2.$$

C.2   Reverse kinematics

The joint angles are given by (C.3) and (C.4)

$$\theta_1 = \arctan\left(\frac{y}{x}\right) \pm \arccos\left(\frac{l_1^2 + x^2 + y^2 - l_2^2}{2l_1\sqrt{x^2 + y^2}}\right) \tag{C.3}$$

$$\theta_2 = \arccos\left(\frac{l_1^2 + l_2^2 - (x^2 + y^2)}{2l_1 l_2}\right). \tag{C.4}$$

D. Detailed joint optimization

This appendix describes the geometry optimization of the compliant joints for the RR mechanism. The goal of the optimization is to maximize the fist unwanted eigenfrequencies of both joints. The method used here has been adopted from [6]. First, an introduction is given to the optimization method. Thereafter, the optimization criteria and input parameters are given. Finally, the modeling method is discussed.

D.1 Introduction

The goal of the optimization is to maximize the first unwanted eigenfrequency of a compliant joint with a given load attached to it. This value is typically given by the lowest second eigenfrequency across the motion range of the joint. The optimization method considered here has been adopted from [6]. This method uses an optimization algorithm in combination with finite element method (FEM) software to tune the parameters that describe the geometry of the considered joint (e.g. length, width, height). To ensure the optimization algorithm produces a feasible design, constraints are specified such as maximum stress and maximum dimensions of components. In summary, the optimization method works as follows:

1. A load is defined to which the joint will be subjected.
2. A set of parameters is selected that describes the geometry of the considered joint.
3. Constraints are defined that solutions returned by the optimization algorithm must satisfy.
4. An optimization algorithm searches for a set of optimal parameters using a FEM program.

D.2 Load case

In general, a load case is given by a mass m, an inertia tensor

$$\underline{J} = \begin{bmatrix} J_{xx} & -J_{xy} & -J_{xz} \\ -J_{xy} & J_{yy} & -Jyz \\ -J_{xz} & -J_{yz} & J_{zz} \end{bmatrix},$$

a vector describing the position of the position of the CoM of the load

$$\underline{r}_{\text{COM}} = \begin{bmatrix} x_{\text{COM}} & y_{\text{COM}} & z_{\text{COM}} \end{bmatrix}^{\text{T}}, \tag{D.1}$$

the gravitational constant $g = 9.81$ m/s^2, and the parameter ϕ that describes the orientation of the load with respect to the joint. The reference frame from which these properties are derived is such that the joint's initial axis of rotation aligns with the vertical (z) axis, and the xy plane aligns with geometric center of the joint, see Figure D.1. The parameter ϕ is used to rotate the load about with respect to this reference frame for optimal alignment with the joint. Note that ϕ rotates the load about the rotation axis of the joint, see Figure D.1. To rotate a load about the vertical axis,
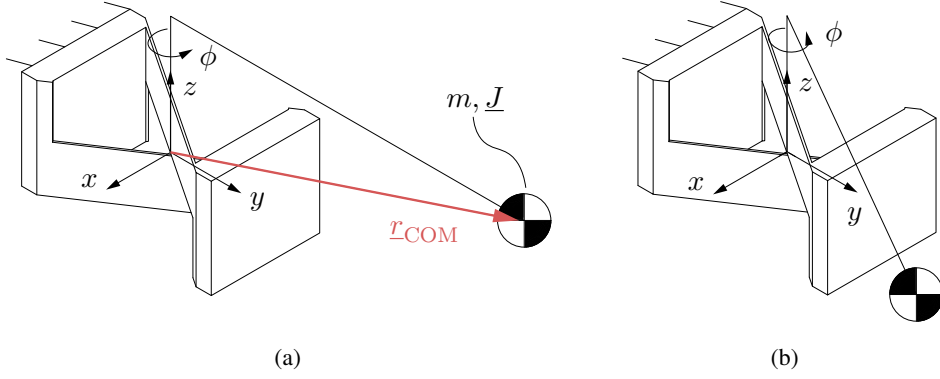
Figure D.1: Visualization load parameters: (a) initial position of the load with respect to the joint, (b) load rotated with about the z axis with parameter ϕ.

the rotation matrix (D.2) has been defined. Using this matrix, the rotated center of mass vector $\underline{r}_{\text{COM}}(\theta_2)'$ and inertia tensor $\underline{J}(\theta_2)'$ are calculated as (D.3) and (D.4) respectively.

$$\underline{R}(\phi) = \begin{bmatrix} \cos(\phi) & \sin(\phi) & 0 \\ -\sin(\phi) & \cos(\phi) & 0 \\ 0 & 0 & 1 \end{bmatrix} \tag{D.2}$$

$$\underline{r}_{\text{COM}}(\theta_2, \phi)' = \left(r_{\text{COM}}^{\text{T}}(\theta_2) \underline{R}_2(\phi) \right)^{\text{T}} \tag{D.3}$$

$$\underline{J}(\theta_2)' = \underline{R}_2(\phi)^{\text{T}} \underline{J}(\theta_2) \underline{R}_2(\phi), \tag{D.4}$$

D.2.1 Variable load

An addition made to the method of [6] is the inclusion of a variable load, as the load of joint 1 is dependent on the orientation of the second arm (θ_2). Note that, as the load is fixed to the moving part of joint 1, the load is not dependent on θ_1. For this variable load, first, the total mass of the RR mechanism is computed as

$$m = m_1 + m_2, \tag{D.5}$$

where m_1 and m_2 denote the mass of the arm 1 and arm 2 respectively. Next, the position of the CoM of arm 2 is derived relative to joint 1 r_{g}. This position is computed using the vector that describes the position of the CoM of of arm 2 relative to joint 2:

$$\underline{r}_{COM2} = \begin{bmatrix} x_{\text{COM2}} & y_{\text{COM2}} & z_{\text{COM2}} \end{bmatrix}^{\text{T}} \tag{D.6}$$

and the vector describing the geometric center of joint 2 for $\theta_1 = 0$, which is dependent on the length of arm 1 L_1 and the height difference between the geometric centers of the joints H_j:

$$\underline{r}_{j2} = \begin{bmatrix} 0 & L_1 & H_j \end{bmatrix}^{\text{T}}.$$

In addition, the rotation matrix $\underline{R}_2$ is defined which is used to rotate the CoM vector with the joint angle θ_2:

$$\underline{R}(\theta_2) = \begin{bmatrix} \cos(\theta_2 - \pi) & \sin(\theta_2 - \pi) & 0 \\ -\sin(\theta_2 - \pi) & \cos(\theta_2 - \pi) & 0 \\ 0 & 0 & 1 \end{bmatrix}.$$

Note that the $-\pi$ term originates from the way how the parameter θ_2 is defined. The vector r_{g} is now computed as:

$$r_{\mathrm{g}} = \underline{r}_{j2} + (\underline{r}_{COM2}^{\mathrm{T}} \underline{R}_2(\theta_2))^{\mathrm{T}} \tag{D.7}$$

Then, the position of the center of mass of the total RR mechanism is computed as

$$\underline{r}_{\mathrm{COM}}(\theta_2) = \frac{1}{m} \big(m_1 \underline{r}_{\mathrm{COM},1} + m_2 \underline{r}_g(\theta_2) \big)$$

$$\underline{J}(\theta_2) = \underline{J}_1 + m_1 \big(\underline{r}_1^{\mathrm{T}} \underline{r}_1 \underline{I} - \underline{r}_1 \underline{r}_1^{\mathrm{T}} \big) + \underline{R}(\theta_2)^{\mathrm{T}} \underline{J}_2 \underline{R}(\theta_2) + m_2 \big(\underline{r}_2^{\mathrm{T}} \underline{r}_2 \underline{I} - \underline{r}_2 \underline{r}_2^{\mathrm{T}} \big),$$

where the subscripts 1 and 2 denote the arm associated with the given parameter and where r_1 and r_2 denote the CoM difference vectors

$$r_1(\theta_2) = r_{\mathrm{COM}}(\theta_2) - r_{\mathrm{COM},1}$$

$$r_2(\theta_2) = r_{\mathrm{COM}}(\theta_2) - r_g(\theta_2).$$

D.3 Optimization

Most optimization algorithms aim at finding a set of variables $\boldsymbol{p}$ for which an objective function $\mathcal{F}(\boldsymbol{p})$ is as small as possible. For this optimization problem, the set $\boldsymbol{p}$ is defined by the geometry parameters of the considered joint. Because the goal is to maximize the lowest second eigenfrequency across the operating range of the joint, the objective function is defined as the inverse of this value

$$\mathcal{F}(\boldsymbol{p}) = \min_Q \big(f_2(\boldsymbol{p}, Q)^{-1} \big) \; \forall \, Q, \tag{D.8}$$

where Q defines the operating range of the joint. For joint 2, this parameter is given by all feasible joint angles $Q = \big\{ \theta_{2,\mathrm{min}} \quad \ldots \quad \theta_{2,\mathrm{max}} \big\}$. For joint 1, Q is defined by all configurations of the joint and RR mechanism (the load) where the end effector lies inside of the workspace:

$$W_x - s_x/2 \leq x \leq W_x + s_x/2$$

$$W_y - s_y/2 \leq y \leq W_y + s_y/2$$

Where x and y denote the end effector position. Furthermore, a set of constraints is defined according to Section 3.2.3

$$\mathcal{C}(\boldsymbol{p}) = \left\{ \begin{array}{c} \max_Q(\sigma(\boldsymbol{p}, Q)) - \sigma_{\mathrm{max}} \\ \max_Q(M(\boldsymbol{p}, Q)) - M_{\mathrm{max}} \\ h - h_{\mathrm{max}} \\ t_{\mathrm{min}} - t \end{array} \right\},$$

for which any solution must comply to $\mathcal{C}(\boldsymbol{P}) \leq 0$. This defines the optimization problem as

$$\boldsymbol{p}_{opt} = \arg \min_{\boldsymbol{p}} \mathcal{F}(\boldsymbol{p}) \text{ subject to } \mathcal{C}(\boldsymbol{p}) \leq 0.$$

Multiple parameters used in this optimization problem are obtained using FEM software, which means that their derivatives with respect to the variables p are difficult to obtain. Therefore, a derivative free optimization algorithm is desired. In addition, this algorithm must be able to solve nonlinear problems as the objective and constraint functions include nonlinearities (such as the maximum stress). The selected algorithm is a Nelder-Mead based solver [15] that has been modified to include constraints. The primary reason for this selection is its efficiency. Other algorithms have also been tested, which gave comparable results. To include constraints in the Nelder-Mead based solver, a penalty function has been used. A penalty λ is generated when a particular constraint is violated. For example, for a maximum stress constraint of $\sigma_{\max}$:

$$\lambda(\boldsymbol{p}) = \begin{cases} 1 \text{ for } \sigma(\boldsymbol{p}) \leq \sigma_{\max} \\ \left(1 + (\sigma - \sigma_{\max})/\sigma_{\max}\right)^3 \text{ for } \sigma(\boldsymbol{p}) > \sigma_{\max} \end{cases}$$

All penalties are multiplied with the objective function to obtain the new objective function

$$\mathcal{F}(\boldsymbol{p}) = \prod_{i=1}^{n} \left(\lambda_i\right) \cdot \min_{Q} \left(f_2(\boldsymbol{p}, Q)^{-1}\right) \forall\, Q, \tag{D.9}$$

where i denotes the penalty corresponding to constraint i and where n is the total number of constraints.

D.4 Modeling

To obtain the eigenfrequencies and constraint parameters, the SPACAR FEM software [16] has been used. This software uses simplified nonlinear beams to simulate mechanical properties of flexible systems. The major advantage of this software with respect to other FEM programs is that it typically runs simulations several orders of magnitude faster, which is desirable when performing many iterations during optimization. The SPACAR models include transverse shear and torsion-extension coupling [16]. The effect of torsion-stiffening is added to the models using the method described in [6].

E. State-of-the-art compliant joints

One of the primary goals of this project was to obtain knowledge about the state of the art large stroke compliant joints used in accurate positioning system. Multiple of these joints have been evaluated in Chapter 3; however, this was not possible for all joints within the time span of this project. The other joints that were found in literature which also have great potential for large stroke applications are listed in this Appendix. The joints described here were shown to be able to have motion range of at least 40°(±20°) and they are claimed to lose a relatively low amount of stiffness when deflected.

Table E.1: Joints from literature and estimated benchmark performance (++: good, +: normal, -: moderate, --: bad). Max parameters denote the maximum values found in literature when applied to a feasible load case. Empty fields are unknown.

Joint	LAFP	Butterfly hinge	Curved Hinge flexure	UT optimized flexure	Cruciform flexure	3 DoF Spherical joint
References	[31]	[11, 32]	[6, 33]	[12, 34]	[35]	[10]
Max motion range	180°	60°	40°	90°	40°	60°tip tilt, 20°pan
Parasitic radial motion	++	+			++	
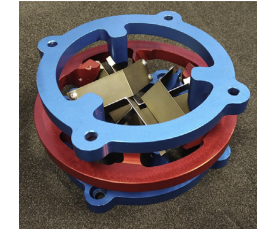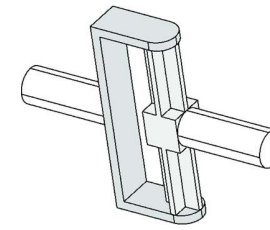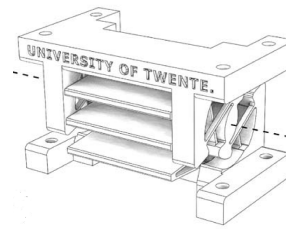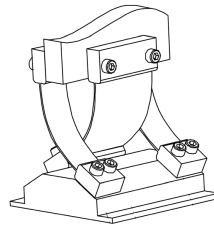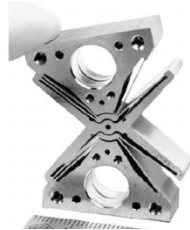
F. Actuator and sensor requirements

In Chapter 5 and 6, actuators and position sensors have been selected for the RR mechanism. To select these components, their performance requirements had to be know, which are derived in this Appendix. Three parameters are derived: first, the maximum rotational velocities of the joints. The actuators and sensors experience the same rotational velocities. Hence, this maximum rotation velocity corresponds to the minimum rotational velocity requirements of these components. Next, the minimum required torques for both actuators is deduced. Finally, the required sensor resolution is deduced.

F.1 Maximum rotational velocities

For the calculation of the rotational velocities, various kinematic parameters are used. See Figure G.1 for the definitions of these parameters if they are unclear.

The maximum rotational velocities of the joints (that are equal to the actuation and sensor velocities) have been deduced from the maximum linear velocity of the printhead during travel motion: $v_{\max} = 0.5$ m/s. Using the reverse kinematic equations that have been derived in Appendix C

$$\theta_1 = \arctan\left(\frac{y}{x}\right) \pm \arccos\left(\frac{l_1^2 + x^2 + y^2 - l_2^2}{2l_1\sqrt{x^2 + y^2}}\right)$$

$$\theta_2 = \arccos\left(\frac{l_1^2 + l_2^2 - (x^2 + y^2)}{2l_1 l_2}\right),$$

the joint velocities have been deduced as

$$\begin{aligned}
\dot{\theta}_1(x, y, \dot{x}, \dot{y}) &= \frac{d}{dt}\theta_1(x, y) \\
&= \dot{x}\left(-\frac{y}{x^2 + y^2} + xA(x, y)\right) + \dot{y}\left(\frac{x}{x^2 + y^2} + yA(x, y)\right)
\end{aligned} \tag{F.1}$$

$$\begin{aligned}
\dot{\theta}_2(x, y, \dot{x}, \dot{y}) &= \frac{d}{dt}\theta_2(x, y) \\
&= \frac{\dot{x}x + \dot{y}y}{l_1 l_2\sqrt{1 - \left(\frac{l_1^2 + l_2^2 - x^2 - y^2}{2l_1 l_2}\right)^2}},
\end{aligned} \tag{F.2}$$

where

$$A(x, y) = \frac{-l_1^2 + l_2^2 + x^2 + y^2}{2l_1(x^2 + y^2)^{\frac{3}{2}}\sqrt{\left(1 - \left(\frac{l_1^2 - l_2^2 + x^2 + y^2}{2l_1(x^2 + y^2)}\right)^2\right)}}.$$

Here, x and y denote the position of the end effector with respect to the rotation axis of joint 1, and $\dot{x}$ and $\dot{y}$ denote the end effector velocities. In the interval were the end effector lies inside of the workspace

$$0.3179 \text{ m} \leq x \leq 0.5422 \text{ m}$$
$$0.0503 \text{ m} \leq y \leq 0.4297 \text{ m}$$

and for

$$v_{\max} \geq \sqrt{\dot{x}^2 + \dot{y}^2},$$

equations (F.1) and (F.2) have the following maxima that define the actuator requirements:

- maximum velocity actuator 1 = 1.82 rad/s,
- maximum velocity actuator 2 = 1.76 rad/s.

The solution to this problem was found using the MATLAB®'fmincon' optimization algorithm. The algorithm returned the same results for many different initial parameters.

F.2 Maximum actuation torques

Two kinds of torque requirements have been specified for each actuator – peak torque, which the actuator must be able to deliver for a short period, and continuous torque. The continuous requirements have been defined as the maximum possible torques during printing motion, where the maximum linear velocity $v_{\max}$= 0.25 m/s and the maximum linear acceleration $a_{\max}$= 5 m/s^2. These maxima represent the torques required for the worst-case end effector trajectory. The peak requirements are given by the maximum possible torques during travel (non-printing) motion, where the maximum linear velocity $v_{\max}$= 0.5 m/s and the maximum linear acceleration $a_{\max}$= 10 m/s^2. Travel motions have a short duration and can therefore use torques that exceed the maximum continuous specifications without overheating the motors.

The torque requirements have been deduced by finding the maximum values of the dynamic equations of the RR mechanism (F.3) and (F.4) that have been derived in Appendix G. Here, τ_1 and τ_2 denote the torques of actuator 1 and 2 respectively, and the generalized coordinates and the corresponding time derivatives are described by

$$q = \begin{bmatrix} \theta_1 & \theta_2 \end{bmatrix}^{\text{T}}, \quad \dot{q} = \begin{bmatrix} \dot{\theta}_1 & \dot{\theta}_2 \end{bmatrix}^{\text{T}}, \quad \ddot{q} = \begin{bmatrix} \ddot{\theta}_1 & \ddot{\theta}_2 \end{bmatrix}^{\text{T}}.$$

$$
\begin{aligned}
\tau_1(q,\dot{q},\ddot{q}) = {} & (J_1 + J_2 + m_2(l_1^2 + l_{cm,2}^2 - 2l_1 l_{cm,2}\cos(\theta_2 - \phi)))\ddot{\theta}_1 + \\
& (J_2 + m_2(l_{cm,2}^2 - l_1 l_{cm,2}\cos(\theta_2 - \phi)))\ddot{\theta}_2 + \\
& m_2 l_1 l_{cm,2}\sin(\theta_2 - \phi)(2\dot{\theta}_1\dot{\theta}_2 + \dot{\theta}_2^2) + k_1(\theta_1 - \theta_{1,0})
\end{aligned}
\tag{F.3}
$$

$$
\begin{aligned}
\tau_2(q,\dot{q},\ddot{q}) = {} & (J_2 + m_2(l_{cm,2}^2 - l_1 l_{cm,2}\cos(\theta_2 - \phi)))\ddot{\theta}_1 + (J_2 + m_2 l_{cm,2}^2)\ddot{\theta}_2 \\
& - m_2 l_1 l_{cm,2}\sin(\theta_2 - \phi)\dot{\theta}_1^2 + k_2(\theta_2 - \theta_{2,0}),
\end{aligned}
\tag{F.4}
$$

61

Similar to the velocity requirements, these maxima were found using Matlab's 'fmincon' optimization algorithm. For this optimization problem, the following constraints have been defined:

$$
\begin{aligned}
W_x - s_x/2 \leq\ & x \leq W_x + s_x/2 \\
W_y - s_y/2 \leq\ & y \leq W_y + s_y/2 \\
\sqrt{\dot{x}^2 + \dot{y}^2} \leq\ & v_{\max} \\
\sqrt{\ddot{x}^2 + \ddot{y}^2} \leq\ & a_{\max},
\end{aligned}
\tag{F.5}
$$

where x and y denote the end effector coordinates with respect to joint 1. In addition, the dot and double dot notations denote the velocities and accelerations respectively. The equations for the The linear velocity and acceleration are given in Appendix C.

The resulting torque requirements are given in Table F.1 and the maximum torque values are plotted over the workspace area of the RR mechanism in Figure F.1. As can be seen in this figure, the maximum torques occur locally, indicating that efficient trajectory planning can significantly reduce the continuously required torques. Further research on efficient trajectory planning is therefore recommended. Refer to Appendix for all physical and geometric properties used in these calculations.

Table F.1: Maximum actuator torques

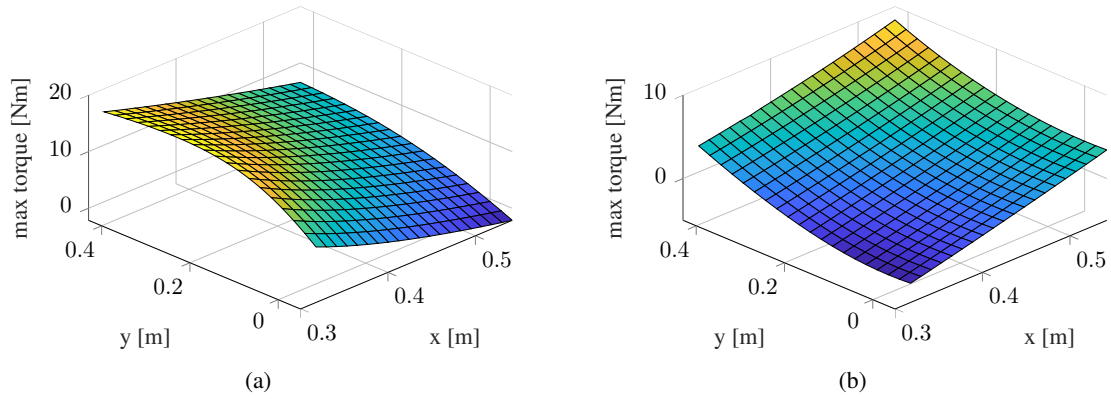|	Continuous	Peak
$\tau_{1,\max}$ [Nm]	16.75	26.67
$\tau_{2,\max}$ [Nm]	8.37	11.89

Figure F.1: Maximum continuous torques plotted across the workspace: (a) actuator 1, (b) actuator 2.

F.3 Measurement system resolution

For the measurement system, the error budget was set to a save value of 10% of the maximum position error of the end effector. The maximum error is specified as 50 µm, hence the budget for the sensors is 5 µm. To estimate the accuracy requirements for the sensors, the configuration of the RR mechanism was taken where $\theta_1 = \theta_2 = 90°$, see Figure F.2. Then, for the analysis of sensor 1, the end effector was shifted 5 µm down as shown in F.2.a. The the resulting angle difference $\Delta\theta_1$ was then considered as the required accuracy for sensor 1. The same configuration of the RR mechanism was considered for the analysis of sensor 2. The end effector was shifted 5 µm right to obtain the joint angle difference $\Delta\theta_2$, which was considered as the accuracy for joint 2. These calculations were performed using the kinematic equations described in C. The resulting for sensor 1 and sensor 2 0.6825 µrad and 0.6022 µrad respectively.

Next, the rotational accuracy is converted to translational accuracy for the linear encoders of the RR mechanism. The minimum radius of encoder scale 1 is 317 mm and that of scale 2 is 235 mm. For sensor 1, this gives a translational accuracy of

$$\text{Accuracy sensor 1} = 0.6825 \cdot 0.317 = 3.78 \mu m$$

end for sensor 2

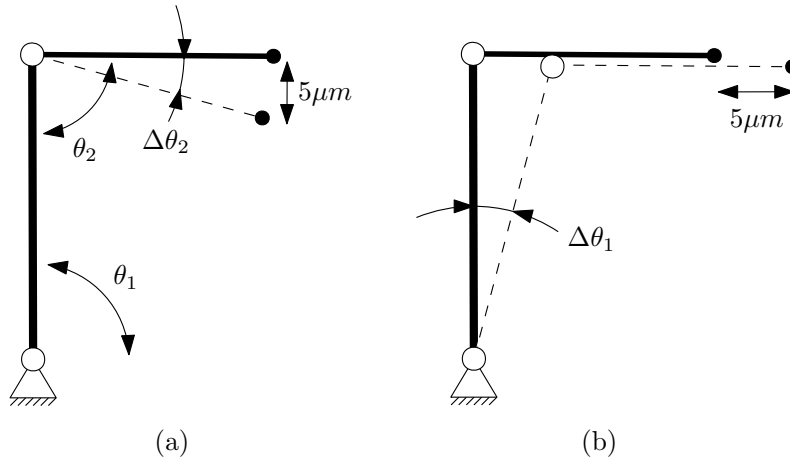$$\text{Accuracy sensor 2} = 0.6022 \cdot 0.317 = 2.47 \mu m.$$

Figure F.2: Sensor analysis configurations

G. Dynamic equations RR mechanism

A simplified dynamic model of the RR mechanism is derived in this appendix using Lagrange mechanics. This model allows to compute the actuator torques for given positions, velocities, and accelerations of both joints. The model is composed of two arms, two joints, and two rotational springs representing the rotational stiffnesses of the compliant joints. Friction, parasitic motions of the joints, and deflections of the arms are not taken into account.

G.1   Introduction

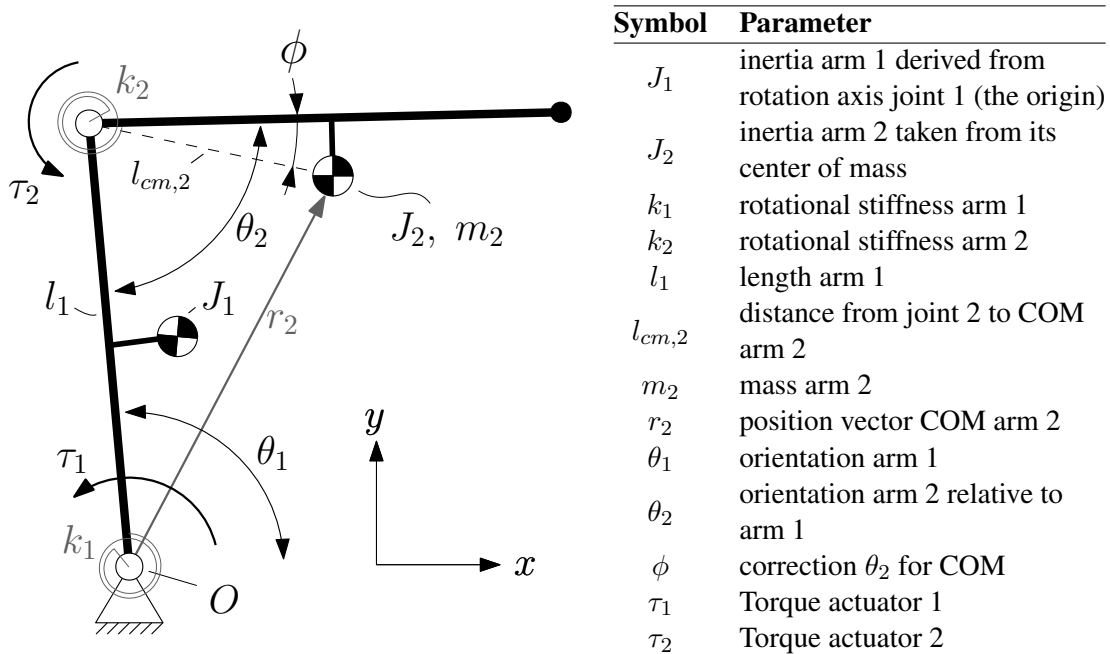| Symbol	Parameter
J_1	inertia arm 1 derived from rotation axis joint 1 (the origin)
J_2	inertia arm 2 taken from its center of mass
k_1	rotational stiffness arm 1
k_2	rotational stiffness arm 2
l_1	length arm 1
$l_{cm,2}$	distance from joint 2 to COM arm 2
m_2	mass arm 2
r_2	position vector COM arm 2
θ_1	orientation arm 1
θ_2	orientation arm 2 relative to arm 1
ϕ	correction θ_2 for COM
τ_1	Torque actuator 1
τ_2	Torque actuator 2

Figure G.1: Parameters dynamic model RR mechanism (top view)

A dynamic model of the RR mechanism has been derived to determine the torque requirements for the actuators driving arm 1 and 2. The model consists of two arms, two joints, and two rotational springs representing the rotational stiffnesses of the compliant joints, as shown in Figure G.1. For simplicity, all masses fixed to the arms are lumped together, including actuator components, sensors, joints, and the end effector. Furthermore, all bodies are considered to be rigid as deflections are not expected to significantly influence the required actuator torques. The compliant joints are modeled as rotational joints with a fixed rotation axis (no parasitic radial motion). Finally, no friction is

taken into account as the joints do not suffer from friction and because no significant aerodynamic friction is expected, as the system operates with a relatively low velocity.

The dynamic model has been derived using the Lagrange equations

$$\frac{d}{dt}\left(T_{,\dot{q}}\right) - T_{,q} + V_{,q} = \begin{bmatrix} \tau_1 \\ \tau_2 \end{bmatrix}, \tag{G.1}$$

where q, T, and V denote the system's generalized coordinates, kinetic energy, and potential energy respectively [36]. Furthermore, τ_1 and τ_2 denote the input torques driving arm 1 and arm 2 respectively. All equations have been derived by hand and were checked using the MATLAB® symbolic toolbox.

G.2 Position and velocity vectors

The selected generalized coordinates are given by the angular parameters

$$q = \begin{bmatrix} \theta_1 & \theta_2 \end{bmatrix}^{\mathrm{T}}.$$

The position vector of the center of mass of the second arm is given by

$$\vec{r}_2 = \begin{bmatrix} l_1 \cos(\theta_1) - l_{cm,2} \cos(\theta_1 + \theta_2 - \phi) \\ l_1 \sin(\theta_1) - l_{cm,2} \sin(\theta_1 + \theta_2 - \phi) \end{bmatrix}.$$

The velocity of the center of mass of the second arm is derived as

$$\dot{\vec{r}}_2 = \frac{d}{dt}\vec{r}_2 = \begin{bmatrix} -l_1 \sin(\theta_1)\dot{\theta}_1 + l_{cm,2} \sin(\theta_1 + \theta_2 - \phi)(\dot{\theta}_1 + \dot{\theta}_2) \\ l_1 \cos(\theta_1)\dot{\theta}_1 - l_{cm,2} \cos(\theta_1 + \theta_2 - \phi)(\dot{\theta}_1 + \dot{\theta}_2) \end{bmatrix}.$$

G.3 Kinetic energy

The kinetic energy of the system is distinguished by the kinetic energy of the first and second arm T_1 and T_2 respectively

$$T_1 = \frac{1}{2}J_1\dot{\theta}_1^2 \tag{G.2}$$

$$T_2 = \frac{1}{2}J_2(\dot{\theta}_1 + \dot{\theta}_2)^2 + \frac{1}{2}m_2\dot{\vec{r}}_2 \cdot \dot{\vec{r}}_2, \tag{G.3}$$

where J_1 denotes the inertia of the first arm taken from the rotation axis of joint 1, J_2 denotes the inertia of the second arm taken from its center of mass, and m_2 describes the mass of the second arm. Note that T_1 does not need a mass velocity term as J_1 represents the inertia of arm 1 taken from the rotation axis of joint 1. Adding (G.2) to (G.3) and working out the $\dot{\vec{r}}_2 \cdot \dot{\vec{r}}_2$ term gives the total kinetic energy of the system:

$$\begin{aligned} T &= T_1 + T_2 \\ &= \frac{1}{2}J_1\dot{\theta}_1^2 + \frac{1}{2}J_2(\dot{\theta}_1 + \dot{\theta}_2)^2 + \frac{1}{2}m_2\big(l_1^2\dot{\theta}_1^2 + l_{cm,2}^2(\dot{\theta}_1 + \dot{\theta}_2)^2 \\ &\quad - 2l_1 l_{cm,2} \cos(\theta_2 - \phi)(\dot{\theta}_1^2 + \dot{\theta}_1\dot{\theta}_2)\big) \end{aligned} \tag{G.4}$$

G.4 Potential energy

The total potential energy in the mechanism is described by the sum of the rotational spring energy of both joints:

$$V = \frac{1}{2}k_1(\theta_1 - \theta_{1,0})^2 + \frac{1}{2}k_1(\theta_2 - \theta_{2,0})^2, \tag{G.5}$$

where $\theta_{1,0}$ and $\theta_{2,0}$ denote the equilibrium (undeflected) orientations of joint 1 and 2 respectively.

G.5 Dynamic equations

Finally, the Lagrange equations are presented which have been derived using (G.1):

$$
\begin{aligned}
\tau_1(q,\dot{q},\ddot{q}) = {} & (J_1 + J_2 + m_2(l_1^2 + l_{cm,2}^2 - 2l_1 l_{cm,2}\cos(\theta_2 - \phi)))\ddot{\theta}_1 + \\
& (J_2 + m_2(l_{cm,2}^2 - l_1 l_{cm,2}\cos(\theta_2 - \phi)))\ddot{\theta}_2 + \\
& m_2 l_1 l_{cm,2}\sin(\theta_2 - \phi)(2\dot{\theta}_1\dot{\theta}_2 + \dot{\theta}_2^2) + k_1(\theta_1 - \theta_{1,0})
\end{aligned}
\tag{G.6}
$$

$$
\begin{aligned}
\tau_2(q,\dot{q},\ddot{q}) = {} & (J_2 + m_2(l_{cm,2}^2 - l_1 l_{cm,2}\cos(\theta_2 - \phi)))\ddot{\theta}_1 + (J_2 + m_2 l_{cm,2}^2)\ddot{\theta}_2 \\
& - m_2 l_1 l_{cm,2}\sin(\theta_2 - \phi)\dot{\theta}_1^2 + k_2(\theta_2 - \theta_{2,0})
\end{aligned}
\tag{G.7}
$$

or in a different form: $\underline{M}(\underline{q})\ddot{\underline{q}} + \underline{H}(\dot{\underline{q}},\underline{q}) = \begin{bmatrix} \tau_1 & \tau_2 \end{bmatrix}^{\mathrm{T}}$, where

$$\underline{M}(\underline{q}) =$$
$$
\begin{bmatrix}
J_1 + J_2 + m_2(l_1^2 + l_{cm,2}^2 - 2l_1 l_{cm,2}\cos(\theta_2 - \phi)) & J_2 + m_2(l_{cm,2}^2 - l_1 l_{cm,2}\cos(\theta_2 - \phi)) \\
J_2 + m_2(l_{cm,2}^2 - l_1 l_{cm,2}\cos(\theta_2 - \phi)) & J_2 + m_2 l_{cm,2}^2
\end{bmatrix}
\tag{G.8}
$$

and

$$
\underline{H}(\dot{\underline{q}},\underline{q}) =
\begin{bmatrix}
m_2 l_1 l_{cm,2}\sin(\theta_2 - \phi)(2\dot{\theta}_1\dot{\theta}_2 + \dot{\theta}_2^2) + k_1(\theta_1 - \theta_{1,0}) \\
-m_2 l_1 l_{cm,2}\sin(\theta_2 - \phi)\dot{\theta}_1^2 + k_2(\theta_2 - \theta_{2,0})
\end{bmatrix}.
\tag{G.9}
$$

H. List of physical and geometric properties of the RR mechanism

For convenience of the reader and for completeness of this thesis, this appendix lists various geometric and physical properties of the RR mechanism.
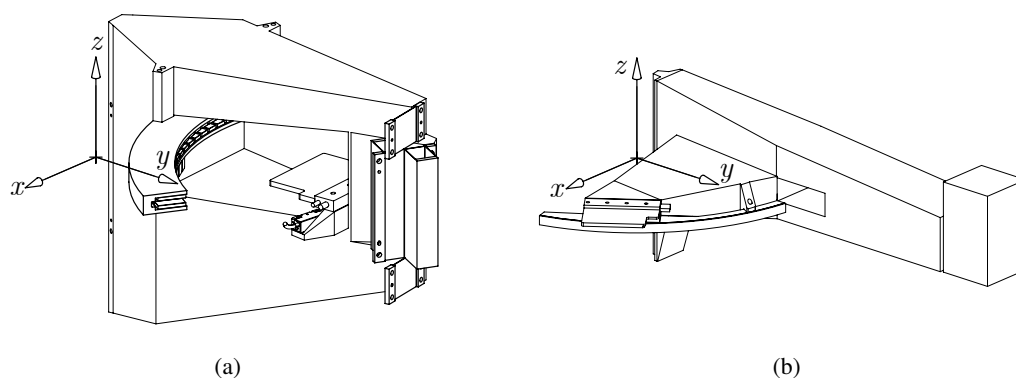

Figure H.1: Arm assemblies with reference frames: (a) arm 1, (b) arm 2

For the properties of arm 1 and 2, the references frames are oriented as shown in Figure H.1. Here, the y axis is aligned collinearly with the longitudinal direction of the corresponding arm. Furthermore, the origins of these reference frames lie in the geometric center of the associated joint. This geometric center lies on the rotation axis of this joint at height= $H_{joint}/2$. The z direction of these reference frames points in the opposite direction of the gravitational force (the vertical direction). The arm 1 assembly consists of: arm 1, joint 2, coil unit 1, magnet yoke 2, and both read heads. Furthermore, the arm 2 assembly consists of arm 2, the coil unit corresponding to actuator 2, the encoder scale corresponding to sensor 2, the end effector. The next page lists the corresponding parameters.

Topology parameters

Parameter	Symbol	Value	Unit	Remark
Length arm 1	l_1	419.71	mm	
Length arm 2	l_2	475.74	mm	
Stroke length in the x direction	s_x	224.31	mm	
Stroke length in the y direction	s_y	480.00	mm	
Workspace center x coordinate	W_x	430.02	mm	w.r.t. joint 1
Workspace center y coordinate	W_y	189.71	mm	w.r.t. joint 1
Height difference geometric center of the joints	H_j	60	mm	

Compliant joints material properties (Stavax)

Parameter	Symbol	Value	Unit	Remark
Young's modulus	E	200	GPa	
Shear modulus	G	80	GPa	
Mass density	ρ	7800	kg/m^3	

Arm 1 assembly properties

Parameter	Symbol	Value	Unit	Remark
Mass	m_1	5.79	kg	
x moment of inertia	$J_{1,xx}$	0.4236	kg m^2	from geometric center of joint 1
y moment of inertia	$J_{1,yy}$	0.0844	kg m^2	from geometric center of joint 1
z moment of inertia	$J_{1,zz}$	0.4174	kg m^2	from geometric center of joint 1
xy product of inertia	$J_{1,xy}$	0.0235	kg m^2	from geometric center of joint 1
xz product of inertia	$J_{1,xz}$	0.0132	kg m^2	from geometric center of joint 1
yz product of inertia	$J_{1,yz}$	0.0819	kg m^2	from geometric center of joint 1
x position CoM	$x_{\mathrm{COM},1}$	19.5	mm	from geometric center of joint 1
y position CoM	$y_{\mathrm{COM},1}$	232.4	mm	from geometric center of joint 1
z position CoM	$z_{\mathrm{COM},1}$	59.6	mm	from geometric center of joint 1
Actuator radius	R_1	286	mm	from rotation axis joint 1

Arm 2 assembly properties

Parameter	Symbol	Value	Unit	Remark
Mass	m_2	1.94	kg	
x moment of inertia	$J_{2,xx}$	0.0531	kg m^2	derived from CoM
y moment of inertia	$J_{2,yy}$	0.0132	kg m^2	derived from CoM
z moment of inertia	$J_{2,zz}$	0.0616	kg m^2	derived from CoM
xy product of inertia	$J_{2,xy}$	-0.0091	kg m^2	derived from CoM
xz product of inertia	$J_{2,xz}$	-0.0008	kg m^2	derived from CoM
yz product of inertia	$J_{2,yz}$	0.0037	kg m^2	derived from CoM
x position CoM	$x_{\mathrm{COM},2}$	43.5	mm	from geometric center of joint 2
y position CoM	$y_{\mathrm{COM},2}$	245.7	mm	from geometric center of joint 2
z position CoM	$z_{\mathrm{COM},2}$	32.1	mm	from geometric center of joint 2
Actuator radius	R_2	250	mm	from rotation axis joint 1

I. Code of scientific conduct

TU/e EINDHOVEN UNIVERSITY OF TECHNOLOGY

Declaration concerning the TU/e Code of Scientific Conduct

I have read the TU/e Code of Scientific Conduct[i].

In carrying out research, design and educational activities, I shall observe the five central values of scientific integrity, namely: trustworthiness, intellectual honesty, openness, independence and societal responsibility, as well as the norms and principles which follow from them.

Date

22 January 2021

Name

Bart Koese

ID-number

1275275

Signature

Submit the signed declaration to the student administration of your department.